Topology Optimization to Design Bone Replacement Shapes in Craniofacial Reconstructive Surgery: Design, Simulation and Experimental Validation

THESIS

Presented in Partial Fulfillment of the Requirements for the Degree Master of Science in the Graduate School of The Ohio State University

By

Jaejong Park

Graduate Program in Mechanical Engineering

The Ohio State University

2013

Master's Examination Committee:

Professor Alok Sutradhar, Advisor

Professor Noriko Katsube

Professor Michael Miller

Abstract

Defects on human facial skeleton caused by blast injury or deformity due to ablation of tumor lead to devastating physical and mental trauma for a patient. Such incidents commonly result in a bone loss in the facial skeleton which destroys structural integrity. Reconstructive surgery is necessary to revive adequate load-transfer mechanism in the facial skeleton, to support the orbital content and to restore functional and aesthetic role. Bone taken from the same patient is often cut and reshaped by osteotomy surgery then placed into the region of bone loss. The surgical outcome therefore not only depends on the size of the defect but also on expertise of the surgeons. Computer aided design with topology optimization which can restore the functions of bone replacements can be a viable alternative. In this research, a state-of-art three dimensional (3D) multi-resolution topology optimization is used to design patient-specific bone replacement shapes for patients with different defects. Bone replacements are inserted into the region of defect using computer-aided design software. Prototypes are fabricated with a 3D printer to explore the mechanical characteristics and behaviors under realistic human mastication loadings. Finite element analysis is also conducted with experimentally obtained printing material properties. Results indicate that topology optimized solutions not only can revive adequate load-transfer mechanism in the facial skeleton but also withstands maximum mastication force found in the literature.

To my family

Acknowledgements

First and foremost, I would like to express the deepest appreciation to my advisor, Professor Alok Sutradhar, for his sincere guidance, support and inspiration. This work would not have been achieved without his patience and encouragement. His passion and endeavor on conducting research have motivated me throughout my graduate studies. Working with him was a truly grateful experience.

I would like to thank Professor Noriko Katsube and Professor Michael Miller who cordially served in my thesis committee and gave perceptive advice and assessment. I gratefully acknowledge the financial support from the National Science Foundation.

I would like to thank Tam Nguyen for his valuable assistance in understanding theories. Thank you to Rich Teynor, Jeremy Seidt for their technical supports during the experiments. I am also grateful to Diana Carrau for her guidance in learning anatomies.

I have boundless gratitude for my parents and sister, Jun Il, Young Nan, and Yang Hee for their absolute faith and confidence in me. Considering their lives and prayers, this accomplishment is nothing but their blessings. It is through their endless care and advocacy that made me stand where I am now. I could not have made it without them. It is my fortune to be part of them as a family.

Vita

2011 ..... B.S. Mechanical Engineering, The Ohio State University

2012 to present ..... Graduate Research Associate, Plastic Surgery, The Ohio State University

Field of Study

Major Field: Mechanical Engineering

Table of Contents

List of Tables

List of Figures

Chapter 1 Introduction

In engineering design, optimization plays a dominant role as it increases reliability and efficiency of the final design. However, classical structural optimization methods such as size and shape optimization are limited in terms of their capability since they only can be applied to predetermined layout i.e. topology. These classical optimization schemes are powerful to basic problems where the designer has a basic idea of the base structures to be optimized by mathematical and deterministic analysis. Even though recent developments in the field of mechanics allow understanding of the characteristics of complex structures, often they are extremely difficult or even impossible to extend the theory to vast majority of real life structural designs.

Topology optimization, a recently developed method can give a viable solution to the design issue because of its ability to suggest the best topology in given domain [1]. It gives where to place materials and where not to which ultimately proposes the optimal number of voids and its shapes in the domain. Topology optimization has gained tremendous attention since its inception [1]. Potential applications of topology optimization are limitless and the ability is still being discovered and developed.

Topology optimization has been successfully applied to a wide variety of engineering problems. One example is the wing box rib design for the Airbus A380 [2]. Aircraft wing box is constructed with number of components including the skin panels,

stringers, spars and the wing box ribs (Figure 1.1). Designing a wing box rib is considered as a local design problem and engineers achieved a significant weight reduction by employing conventional energy based topology optimization algorithm.

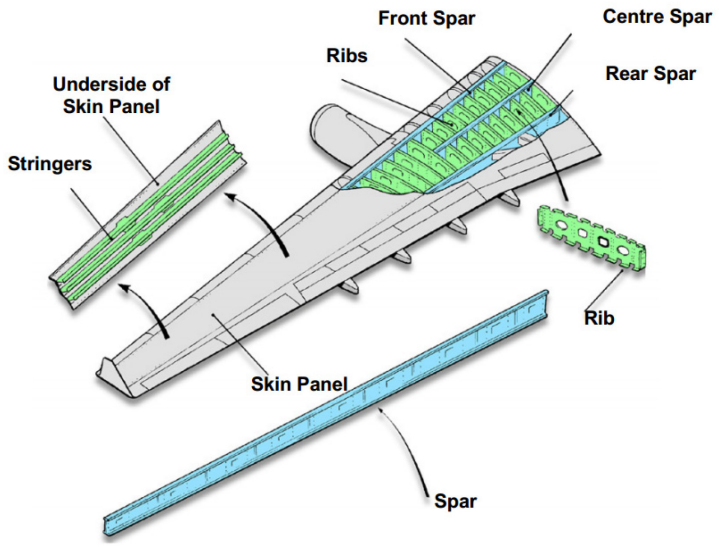

Figure 1.1. Main components in commercial aircraft wing box [2]

In this thesis, topology optimization is used to creating bone replacement shapes for craniofacial reconstructive surgery. Bone replacement shapes for various types of patient's defects are modeled and designed using the topology optimization approach. Then, feasibility of proposed solutions is investigated from both clinical and engineering standpoint by conducting finite element analysis and mechanical testing on their prototypes. Human mastication with maximum reported force possible is simulated for verification and validation purpose.

1.1 Topology Optimization

Every structural object experiences stress when loaded and because of the stress, the structure changes its shape as a response to the load to be in the best equilibrium status as explained. In practice, structural optimization methods are introduced to obtain enhanced design with increased efficiency. Classical structural optimization methods include size, and shape optimization. Figure 1.2 depicts the design of bridge-like structure in a 2D domain. In this problem, sizing optimization determines the best size or thickness of structure or its components whereas shape optimization trims pre-determined design to suggest better design. The condition in common on these classical structural optimization methods is that an initial design needs to be included as an input to the method. Topology optimization can be considered as a combination of classical structural optimization without the necessity of a predefined design since it aims to find optimal distribution of material to shape an optimized structure in a specific domain while satisfying given design constraints. The concept of topology optimization was first introduced by Bensøe & Kikuchi in 1988 with an intention to develop an algorithm to design linear elastic structures with minimum weight possible [3]. It incorporated the finite element analysis into optimization scheme and the design variables i.e. densities in each element were used to analyze and represent the final topology.

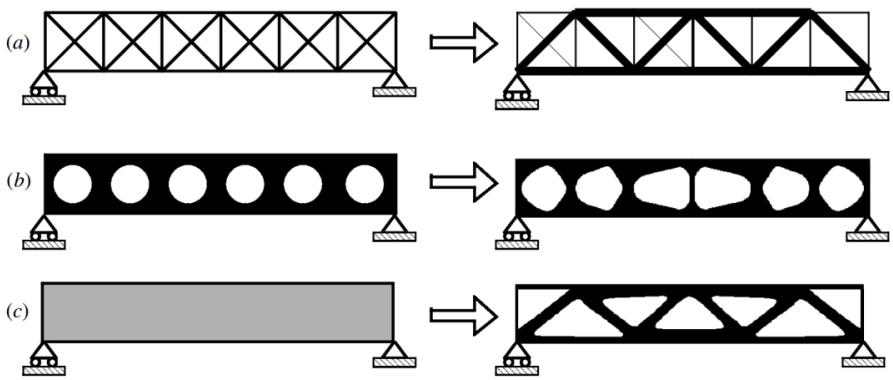

Figure 1.2. Structural optimization: (a) Size optimization
(b) Shape optimization (c) Topology optimization [4]

In finite element analysis based topology optimization elemental density is assigned either zero or unity. However, then it becomes a discrete integer optimization which makes the algorithm computationally undesirable. Thus, in topology optimization, densities are allowed to have intermediate values between 0 and 1 to have continuous objective and constraints that are differentiable as well as solution convergent. Earlier topology optimization methods used homogenization method [3, 5] to calculate element properties with intermediate densities. In order to improve reliability of solutions, another approach named "power-law approach" or SIMP (Solid Isotropic Material with Penalization) was proposed [6, 7]. In SIMP, the intermediate density values follow a power-law to direct them to upper and lower bounds. Later, it was proved that SIMP model is permissible when a certain condition is met on power factor. [7]

Topology optimization can provide ill-posed solution because it does not give unique solution due to the nature of finite element analysis. The solution depends on the meshing of the design domain in finete element analysis. Thus, a solution from topology optimization is also mesh dependent. Numerical instabilities such as checker board

pattern comes from the same reason [8]. Topology optimization is not preferred in large scale problems because it demands computationally expensive large scale finite element analysis. Methods to tackle this issue have been suggested in a great number of literatures and which can be categorized into three groups. First is adhoc approach and it uses parallel computing to overcome computing cost of analyzing fine meshes [9, 10]. Second aims to reduce computing cost by approximating response and does finite element analysis periodically [11] or by employing efficient solvers [12, 13]. Last method decouples the finite element analysis with the optimization scheme by making design variable not coincide with finite element mesh [14-16]. Choosing right approach for design variable with projection functions, aforesaid inherent drawbacks of element-based topology optimization can be avoided.

1.2 Topology Optimization in Biomedical Science

There exist over two hundred bones in human skeleton. Each of them are located and connected in various ways to support and protect organs and soft tissues nearby in order to establish a structural form of human. Therefore, each bone has different complex macro and micro configurations to achieve their own roles. Bone tends to fail under sudden impact, loads in large magnitude or fatigue in the form of fracture or degradation. Bones are often surgically removed due to tumor metastasis or bone-related diseases. Reconstructive surgery is necessary for injuries with large bone loss to restore normal function and appearance and this is very important task because it is directly related to maintaining quality of life of the patient.

Surgical outcome can be enhanced from taking an interdisciplinary approach. In fact, the foremost important step in reconstructive surgery is rather obvious. It is to

design a bone replacement that would qualitatively fulfill the 4Fs: Form, Function, Fixation, and Formation [17]. Bone replacement scaffold needs to properly fill the region of defect (form), bear the mechanical loading (function), be securely settled so that further loosening (pseudarthrosis) can be avoided (e.g., fixation) while it helps tissue formation by supporting nutrition transport and deliver (formation).

Topology optimization can be considered as guidance that aids achieving objectives of the aforementioned 4Fs. Substantial studies have been already conducted via topology optimization to design microstructures that enhances formation requirement with different pore sizes [18-20], hierarchical scaffold [21]. In order to improve the biomechanical environments, various material properties such as elasticity that matches bone [22], bulk modulus and diffusivity [23] anisotropy of bones [24] were proven to be crucial as well. Also, algorithm for making scaffold degradable after appropriate healing (tissue regeneration) is examined [25].

Designing a scaffold that meets all 4F requirements simultaneously is not yet possible and it is known to be very challenging. Knowing this, the plan of the work is to achieve each category in 4Fs one at a time and investigate any potential of combining them along the way.

1.3 Craniofacial Reconstruction Surgery

Restoration process becomes significantly difficult when bone loss occur in the human facial skeleton. Schultz claims, "*Man's face is his single most distinguishing physical characteristic. It is at once the key to his identity and his primary means of communicating both thought and emotion.*" [26]. That is, facial skeleton represents each

person's characteristic. Inadequate surgery can result in devastating consequences for the suffering individual. Based on the size, segmental bone defects of the midface require bone grafts for a successful outcome. This still remains an unsolved problem in craniofacial reconstruction surgery. The most reliable current technique for restoring such defect is making the use of autologous bone, fibula for example, after osteotomies to obtain proper structure (Figure 1.3). Yet, the outcome of this heuristic method depends on each surgeon's skills and experience and it does not guarantee post-surgery structural integrity in the facial skeleton.

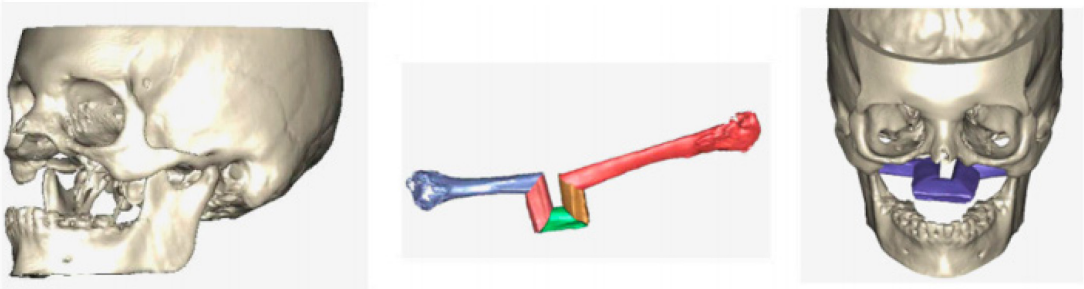

Figure 1.3. Current technique for craniofacial reconstructive surgery [27]

From the mechanics point of view, the main goal is to restore primary load transfer mechanism that is responsible of smooth flow of stresses from loadings such as mastication. Topology optimization is a promising method because such buttress system can be reproduced when appropriate boundary conditions are used [27]. This approach will ensure that the topology optimization solutions meet form and functional requirements of Hollister's 4Fs (form, function, fixation, and formation).

1.4 Research Objectives and Thesis Organization

The present work focuses on the studying the feasibility of designing the shapes of patient-specific bone replacements especially for large craniofacial injuries. The original concept of using topology optimization to design bone replacements in craniofacial reconstruction is presented by Sutradhar [27]. In [27], the idea is verified with 2D topology optimization and 3D topology optimization algorithm is used to obtain the topology of bone implants for a gunshot injury in the midface.

In the current work, the algorithm suggested by Sutradhar is applied to various kinds of defects from patient image data to suggest respective topology optimized bone replacement shapes. These topology optimized solutions are inserted in the defect using computer aided design tool and their skull models are fabricated with 3D printing technique and meshed to generate finite element model to explore their mechanical feasibility through finite element analysis and mechanical testing under simulation of realistic human mastication.

This thesis is organized as follows. Chapter 2 explains the formulation of topology optimization and introduces multiresolution topology optimization which is the method employed for this work followed by numerical examples. Patient data, topology optimization application and its solutions are shown in Chapter 3 along with parametric study of design variables for multiresolution topology optimization. Validation of the work is presented in Chapters 4 via finite element analysis and appropriate mechanical testing of selected solution under human mastication simulation. Finally, Chapter 5 summarizes the key notes of the research and shows plans for future work.

Chapter 2 Basics of Topology Optimization

This chapter explains the basic formulation of traditional topology optimization for minimizing compliance and discusses its strengths, drawbacks and weaknesses. The effort to resolve the shortcomings are discussed. A multi-resolution topology optimization method that is employed for this work is introduced. It is compared to traditional topology optimization using two dimensional and three dimensional examples.

2.1 Introduction

Topology optimization is most advanced technique among structural optimization methods because it aims optimal material distribution within a domain; sizing and shaping of voids are integrated within the algorithm [4]. The algorithm is iterative and is consists of two distinct modules; one for analysis and the other for optimization. In each iteration, finite element analysis is conducted over the solution to find the structural behavior. Thus topology optimization requires discretization of domain and the solution is greatly dependent upon the way it is discretized. This issue arises as problems in topology optimization in the form of mesh independency and checkerboard patterns [8]. There have been significant studies to address these issues including using filters [28]. Also, to achieve higher fidelity of solutions, multi-resolution topology optimization scheme [29] is used.

2.2 Problem Formulation

In continuum structures, topology optimization determines the best material distribution in a specific domain. Minimization of compliance while satisfying a volume constraint is considered as the objective in the algorithm for this study. Consider a reference domain Ω with boundary Γ in $\mathbf{R}^2$ or $\mathbf{R}^3$, under $\mathbf{b}$ the body forces and $\mathbf{t}$ the traction. The aim is to find the optimal choice of stiffness tensor $E_{ijkl}(x)$ where x denotes the position. Then, the energy bilinear form at equilibrium $\mathbf{u}$ with arbitrary displacement $\mathbf{v}$ can be written as $a(\mathbf{u},\mathbf{v})=\int_\Omega E_{ijkl}(\mathbf{x})\varepsilon_{ij}(\mathbf{u})\varepsilon_{kl}(\mathbf{v})d\Omega$, where $\varepsilon_{ij}(\mathbf{u})=\frac{1}{2}\left(\frac{\partial u_i}{\partial x_j}+\frac{\partial u_j}{\partial x_i}\right)$ is the linearized strain, and load linear form is $L(\mathbf{u})=\int_\Omega \mathbf{b}\mathbf{u}d\Omega+\int_\Gamma \mathbf{t}\mathbf{u}ds$. The basic minimum compliance problem is in the form of,

$$\begin{aligned} &\text{minimize: } L(\mathbf{u}) \\ &\text{subject to: } a(\mathbf{u},\mathbf{v})=L(\mathbf{v}), \text{ for all } \mathbf{v}\in U \\ &\qquad\qquad \text{and volume constraint} \end{aligned} \tag{2.1}$$

here U denotes the space of kinematically admissible displacements and the equilibrium equation is in the weak, variational form [4]. In order to utilize the formulation in topology optimization, (2.1) is discretized using finite element method. The objective of minimizing compliance is achieved by assigning optimum density values in each element over the discretized domain. Therefore, element density values are the design variable in the formulation. Topology optimization formulation is shown in (2.2).

$$\underset{\rho}{\text{minimize:}}\ C(\boldsymbol{\rho},\mathbf{u}) = \mathbf{f}^T\mathbf{u}$$

$$\text{subject to: } \mathbf{K}(\boldsymbol{\rho})\mathbf{u}=\mathbf{f} \qquad \textbf{(2.2)}$$

$$\text{Volume constraint } V(\boldsymbol{\rho}) = \int_\Omega \boldsymbol{\rho}(x)dV \le V_s$$

where C is the compliance, **ρ, f** and **u** are density, global load and displacement vectors respectively. V_s is the volume constraint. **K** is the global stiffness matrix which depends on **ρ** that determines element stiffness $\mathbf{K}_x$. Therefore, **K** can be rewritten as,

$$\mathbf{K} = \sum_{x=1}^{N_{el}} \mathbf{K}_x(\rho_x) = \int_{\Omega_x} \mathbf{B}^T\mathbf{D}(\rho_x)\mathbf{B}d\boldsymbol{\Omega} \qquad \textbf{(2.3)}$$

where **B** is the shape function derivatives, and **D** is the material property matrix that depends on element density taken from stress-strain relationship. Step by step derivation of **B** and **D** (plane stress) is provided in the appendix for a standard four noded quad (Q4) element.

One notices that the formulation shown in (2.2) must allocate density value of discrete 0 (void) or 1(solid) at any element in the domain. This distributed, discrete valued optimization problem is computationally undesired. Common approach to circumvent this intractability is to replace integer options for density to continuous variables. That is, the problem is relaxed for density to have any intermediate values between 0 and 1. A small lower bound ($\rho_{min} = 10^{-3}$) is inserted to avoid singularity when solving for equilibrium in domain Ω. In addition, if intermediate density values are

penalized, they are steered to converge to either extreme that original formulation (2.2) is aimed for. With this approach, material property of an element at location x is expressed as follows.

$$\mathbf{E_{ijkl}}(x)=\boldsymbol{\rho}(x)^{p}\mathbf{E_{ijkl}}^{0} \tag{2.4}$$

where $\mathbf{E_{ijkl}}^{0}$ is the solid phase ($\rho = 1$) material property of element at location x and p is the penalization factor. In fact, this widely known technique called SIMP (Solid Isotropic Material with Penalization) model [6, 7] was critiqued since it introduces artificial material into the problem [30] but it was soon discovered that if penalization factor is sufficiently large e.g. ($p \geq 3$), SIMP model satisfies Hashin-Shtrikman bounds and thus satisfactory [7]. The material matrix **D** shown in (2.3) for plane stress takes the form shown in (2.5).

$$\mathbf{D}(x)=\frac{\mathbf{E_{ijkl}}(x)}{1-\nu^2}\begin{bmatrix}1 & \nu & 0\\ \nu & 1 & 0\\ 0 & 0 & (1-\nu)/2\end{bmatrix} \tag{2.5}$$

Also, since the problem is relaxed for density to be located anywhere between lower bound ρ_{min} and 1, sensitivities with respect to design variable of the objective function and constraints needs to be computed for gradient-based optimization in (2.2). Recognizing ρ is the design variable for this specific material distribution problem, sensitivities can be computed as follows

$$\frac{\partial C}{\partial \rho_e} = -\mathbf{u}_e{}^T \frac{\partial K_e}{\partial \rho_e} \mathbf{u}_e = -p(\rho_e)^{p-1} \mathbf{u}_e{}^T \mathbf{K}_e{}^0 \mathbf{u}_e$$

$$\frac{\partial V}{\partial \rho_e} = \int_{\Omega_e} dV \tag{2.6}$$

However, this element based optimization has drawbacks. The goal is to assign optimal density value in each element and this can lead to regions where solid and void elements are alternating without clear connectivities between them. This checkerboard pattern may lead to unacceptable solutions. It also does not give qualitatively the same solution for different mesh sizes [8] due to finite element analysis that the algorithm incorporates. These checkerboard pattern and mesh dependence can be eliminated to a certain degree by using filter [8, 28]. In general, filter searches circular region for 2D and spherical region for 3D, then manually modifies the elemental sensitivities such that density contour has continuous gradient over the domain. This follows the algorithm shown in (2.7) and **Figure 2.1** (for bilinear quadrilateral (Q4) elements).

$$\frac{\partial C}{\partial \rho_x} = \frac{1}{\rho_x \sum_{j=1}^{N} \hat{H}_j} \sum_{j=1}^{N} \hat{H}_j \rho_j \frac{\partial C}{\partial \rho_j}$$

$$\hat{H}_j = r_{min} - dist(x,j) \tag{2.7}$$

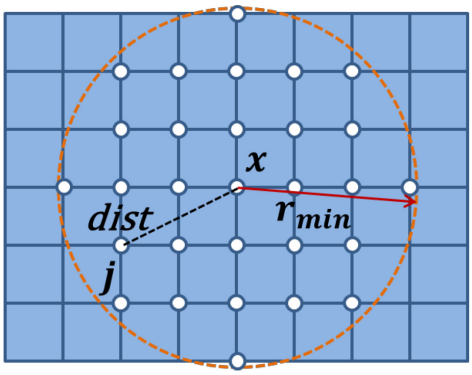

Figure 2.1. Calculation of convolution operator $\hat{H}_j$ in 2D

This filtering technique suppresses the checkerboard pattern and alleviates mesh independency depending upon filter radius r_{min}. Example in Figure 2.2 shows the effect of filter in a cantilever beam subjected to a vertical load.

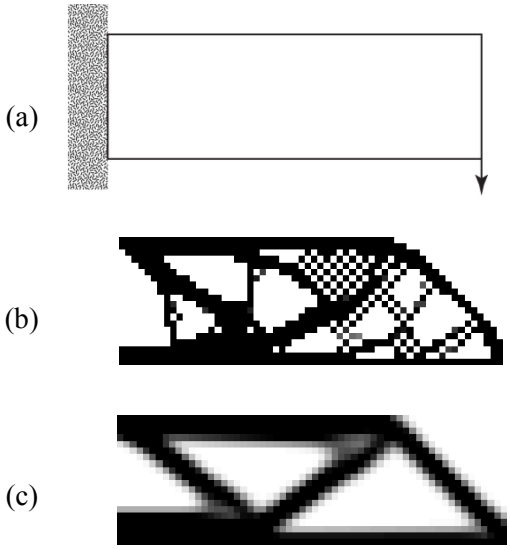

Figure 2.2. Effect of filter on the solution of a cantilever beam problem:
(a) Design problem (b) Topology optimized design w/o filter
(c) Topology optimized design with filter (r_{min}=2)

Once the sensitivities are modified with filter, the design variables (i.e. densities for minimum compliance problem) are updated based on element sensitivities. There exist a number of updating methods for structural optimization including Methods of Moving Asymptotes (MMA) [31] and Optimality Criteria (OC) [32]. Upon choosing Optimality Criteria as optimizer over MMA due to its computation speed advantage for simple compliance problems [4], update scheme can be established from the Lagrangian function (2.8) of the problem statement in (2.2).

$$L = \mathbf{u}^T\mathbf{K}\mathbf{u} + \lambda_1^T\cdot(\mathbf{K}\mathbf{u} - \mathbf{F}) + \lambda\cdot(V - V_s) \tag{2.8}$$

which provides optimality condition of $B_x = \left(-\frac{\partial C}{\partial \rho_x}\right)/\lambda$. Here, the Lagrangian multiplier heuristically λ is found by a bi-section method to match the volume constraint. Adapting a numerical damping coefficient of $\eta = 1/2$ to stabilize the iteration with appropriate modifying limit *move*, updating scheme evolves as follows,

$$\rho_x^{k+1} = \rho_x^k\cdot\left(B_x^k\right)^\eta$$

$$\begin{aligned}
&\text{if } \rho_x^k\cdot\left(B_x^k\right)^\eta \le \rho_{min} && \rho_x^{k+1} = \max(\rho_x^k - move,\ \rho_{min})\\
&\text{if } \rho_x^k\cdot\left(B_x^k\right)^\eta \ge 1 && \rho_x^{k+1} = \min(\rho_x^k + move,\ 1)\\
&\text{else} && \rho_x^{k+1} = \rho_x^k\cdot\left(B_x^k\right)^\eta
\end{aligned} \tag{2.9}$$

where *k* represents the iteration number.

Iterative, gradient and element based topology optimization algorithm discussed in this section can easily be summarized with a flowchart shown in Figure 2.3.

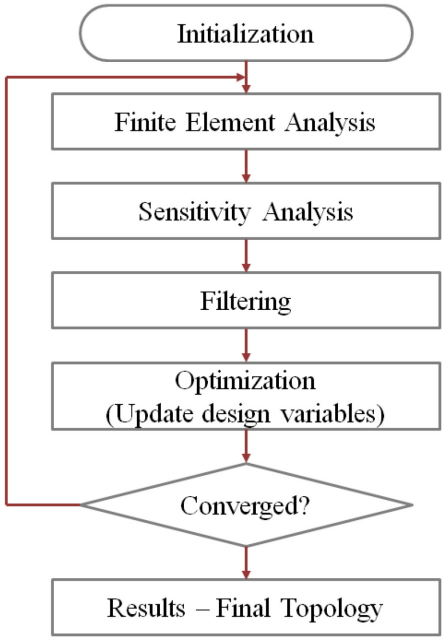

Figure 2.3. Flow chart of topology optimization

2.2 Efficient and Accurate Solution for Topology Optimization

With finer discretization that represents the design domain, the resolution of the solution is higher which leads to better visualization and higher fidelity. However, with increased number of elements for computer to handle, required CPU time gets exponentially longer with potential demand in parallel computing. This can be avoided by reducing computational cost directly with 'fast iterative solvers' to reduce the calculation time associated with finite element analysis [33]. Also, Amir et al. (2009) proposed approximate reanalysis method that performs finite element analysis

periodically and approximates the displacement in the iteration that finite element analysis is skipped [11]. Abovementioned method utilizes displacement mesh for finite element analysis and coarser density mesh shown in Figure 2.4. However, by employing finer configuration for design variables, it is possible to get solutions with higher resolution. That is, instead of using design variables as densities of each element, nodal densities can be considered as design variable [14, 15, 34]. In these studies, element densities for finite element analysis in next step are calculated from nodal densities via projection functions which are equivalent to filters.

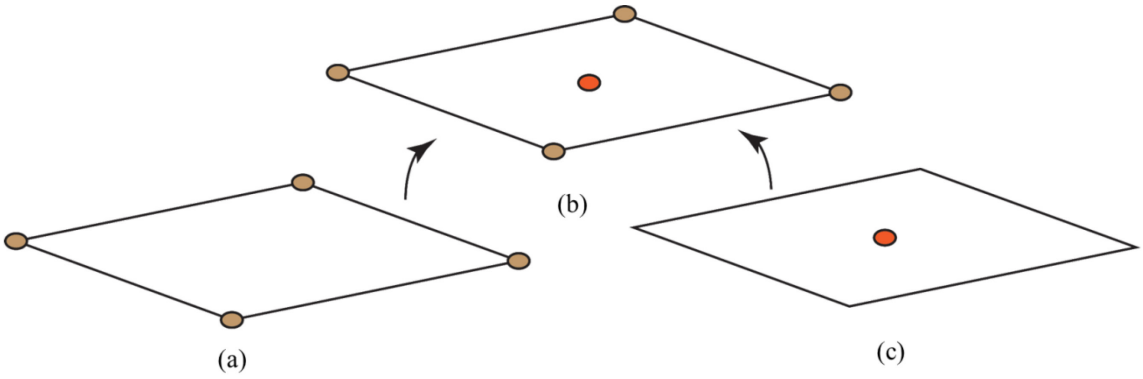

Figure 2.4. Element-based approach (Q4/U):
(a) Displacement mesh, (b) Superposed mesh, (c) Density mesh

A recent study by Nguyen et al. [29] introduces multiple levels of meshes for different computation components that gives solutions with even higher resolution with relatively low computational cost. Nguyen [29] proposed the Multiresolution Topology Optimization (MTOP) to assign coarse mesh for rather computational expensive finite

element analysis and finer meshes to design variable and density mesh to enhance visualization. The algorithm multiresolution topology optimization assigns three different meshes as shown in Table 2.1 and Figure 2.5.

Table 2.1. Multiresolution topology optimization mesh assignment

Mesh	Purpose
Finite element	Stress-strain analysis
Design variable	Optimization
Density	Stiffness matrix calculation, Visualization

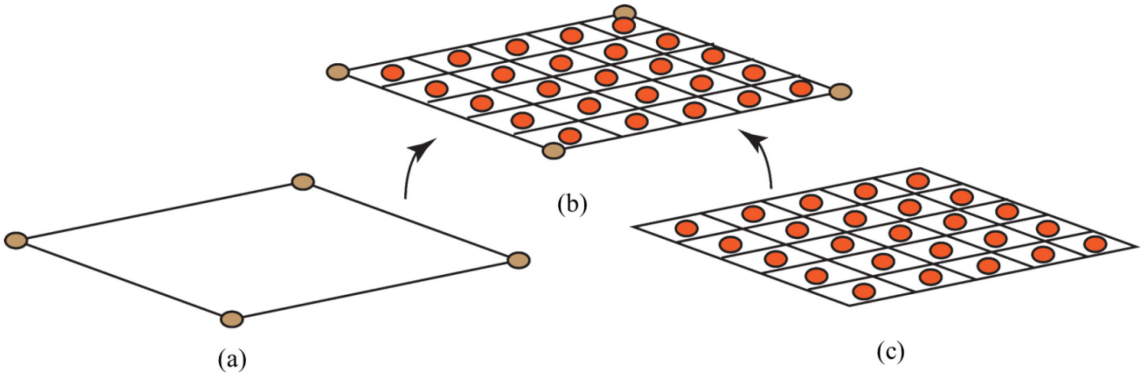

Figure 2.5. Multiresolution topology optimization approach (Q4/n25):
(a) Displacement mesh (b) Superposed mesh (c) Design variable mesh

Upon comparing mesh densities for element based approach with multiresolution topology optimization with Q4/n25 element, the resolution of multiresolution topology optimization with Q4/n25 element scheme is twenty five times finer. Figure 2.6 is the illustration of potential spatial variation of the density in single conventional Q4/U element and multiresolution topology optimization Q4/n25 element.

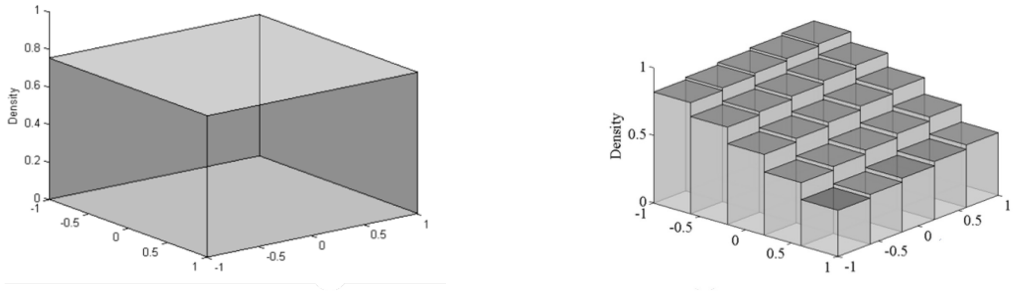

(a) (b)

Figure 2.6. Density spatial variation in a single displacement element:
(a) Conventional Q4/U element
(b) Multiresolution topology optimization Q4/n25 element [29]

In original formulation in (2.2), single value represents the density inside a displacement element. However, since there is a set of density values in a displacement element of multiresolution topology optimization that are controlled by a projection function, formulation undergoes minor modification. The mathematical formulation and methods are described next [29]. The projection function is included as an extra constraint and the problem can be rewritten as follows

$$\begin{aligned} &\underset{\rho}{\text{minimize:}}\ C(\rho,\mathbf{u}) = \mathbf{f}^T\mathbf{u} \\ &\text{subject to: } \rho = f_p(\mathbf{d}) \\ &\qquad\qquad \mathbf{K}(\rho)\mathbf{u}=\mathbf{f} \\ &\qquad\qquad V(\rho)=\int_\Omega \rho(x)dV \le V_s \end{aligned} \tag{2.10}$$

where f_p is the projection function and $\mathbf{d}$ is the design variable array. Stiffness matrices of any multiresolution topology optimization elements are obtained by adding all stiffness of all relevant density elements. Employing SIMP model, element stiffness matrix calculation follows algorithm shown below

$$\mathbf{K}_e(\rho_e)=\int_{\Omega_e}\mathbf{B}^T\mathbf{D}(\rho_e)\mathbf{B}d\boldsymbol{\Omega}=\sum_{i=1}^{N_n}\left(\int_{\Omega^i{}_e}\mathbf{B}^T\mathbf{D}\mathbf{B}d\Omega^i{}_e\right)$$

SIMP: $$\mathbf{K}_e(\rho_e)=\sum_{i=1}^{N_n}(\rho_i)^p\left(\int_{\Omega^i{}_e}\mathbf{B}^T\mathbf{D}^0\mathbf{B}d\Omega^i{}_e\right) \quad \textbf{(2.11)}$$

where i is the element number and $\mathbf{D}^0$ is the material property matrix at solid phase. Sensitivity analysis of the new compliance in (2.10) requires sensitivity of modified stiffness matrix as (2.12).

$$\frac{\partial\mathbf{K}_e}{\partial d_n}=\frac{\partial\mathbf{K}_e}{\partial\rho_i}\frac{\partial\rho_i}{\partial d_n}=\frac{\partial\sum_{j=1}^{N_n}(\rho_i)^p\mathbf{I}_j}{\partial\rho_i}\frac{\partial\rho_i}{\partial d_n}=-p(\rho_i)^{p-1}\mathbf{I}_i\frac{\partial\rho_i}{\partial d_n} \quad \textbf{(2.12)}$$

Also, projection function presented by $\rho = f_p(\mathbf{d})$ in (2.10), the sensitivity of volume constraint is in the form of (2.13).

$$\frac{\partial V}{\partial d_n}=\frac{\partial V}{\partial\rho_i}\frac{\partial\rho_i}{\partial d_n} \quad \textbf{(2.13)}$$

where the term $\frac{\partial \rho_i}{\partial d_n}$ is obtained from projection function. Employing polynomial projection function (Figure 2.7), each density element is assigned with a value that comes from taking weighted average of the nearby design variables as shown in (2.14).

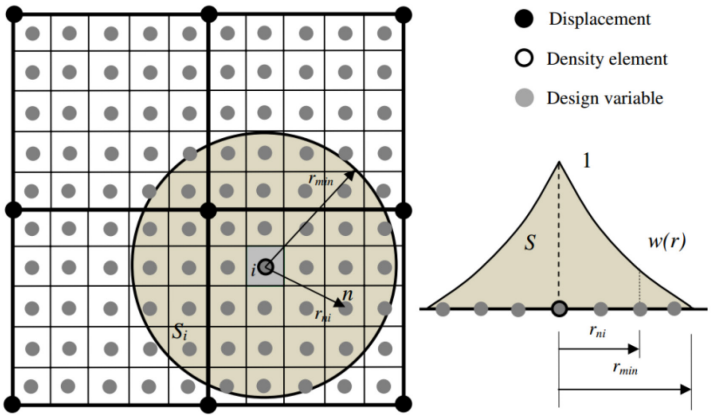

Figure 2.7. Projection function from the design variables to the density element [29]

$$\rho_i = \frac{\sum_{n \in S_i} d_n w(x_n - x_i)}{\sum_{n \in S_i} w(x_n - x_i)} \tag{2.14}$$

here, S_i represents the sub-domain of i^{th} density element, x_n is the point location of design variable d_n, and the definition of weight factor $w(x_n - x_i)$ is presented in (2.15).

$$w(x_n - x_i) = \begin{cases} \frac{r_{min} - r_{ni}}{r_{min}} & \text{if } r_{ni} \le r_{min} \\ 0 & \text{otherwise} \end{cases} \tag{2.15}$$

Finally, the sensitivity of element density induced via projection function with respect to design variable $\frac{\partial \rho_i}{\partial d_n}$ is obtained as follows

$$\frac{\partial \rho_i}{\partial d_n} = \frac{w(x_n - x_i)}{\sum_{n \in S_i} w(x_n - x_i)} \tag{2.16}$$

Since multiresolution topology optimization introduces denser mesh for design variable and density, it does require extra CPU time when compared to element based topology optimization formulation in (2.2) [29]. However, that additional time demand compensates with solution with far better (25 times finer with Q4/n25 than traditional Q4) resolution efficiently than employing large set of elements directly in (2.2). Nguyen *et al.* also discovered that the calculated compliance converges very well with element based topology optimization [29].

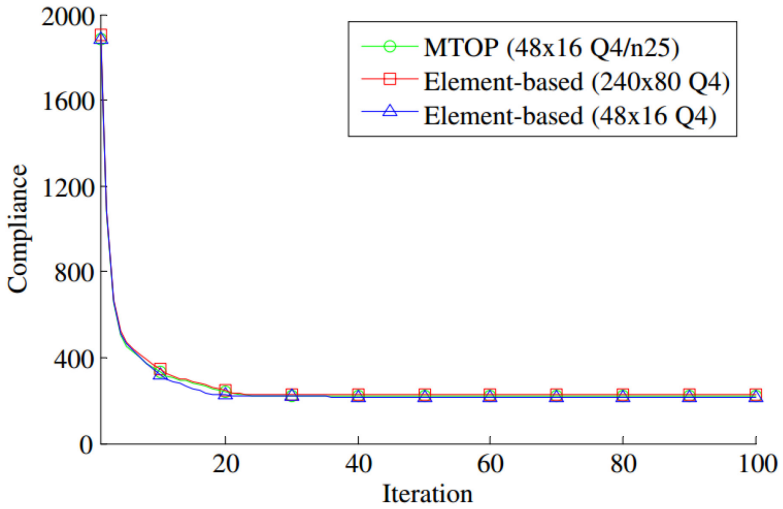

Figure 2.8. Convergence history after 100 iterations [29]

Additionally, the multiresolution topology optimization algorithm can be easily expanded to three dimensional problems. B8/n125 is the 3D equivalent of the 2D Q4/n2 elements. That is, there are 125 design variables that shape the topology of local displacement element. Numerical results of various problems in both 2D and 3D via element based topology optimization and multiresolution topology optimization are compared and discussed in section 2.3.

2.3 2D and 3D Numerical Examples: Cantilever Beam

Element based topology optimization and multiresolution topology optimization are applied to a simple 2D cantilever beam problem. The design domain is discretized so that there exist 16 displace elements along the height and 48 displace elements in lengthwise direction totaling 768 Q4 elements as shown in Figure 2.9. A downward unit force is applied in the middle of right end.

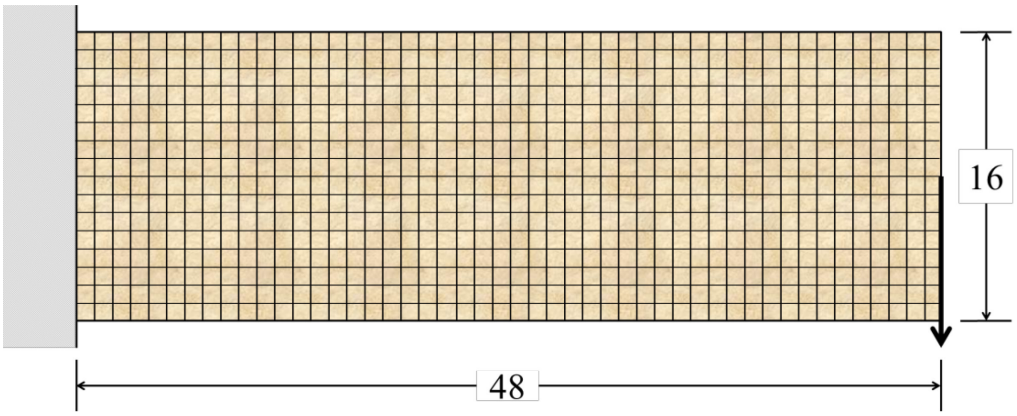

Figure 2.9. 2D cantilever beam problem

The same design variables of 50% volume fraction (V_s), filter size (r_{min}) of 1.2, and penalization power (p) of 4 are selected and employed in both techniques. The result from same discretization of design domain shows that the resolution of solution with multiresolution topology optimization is much higher than that with element based topology optimization (Figure 2.10).

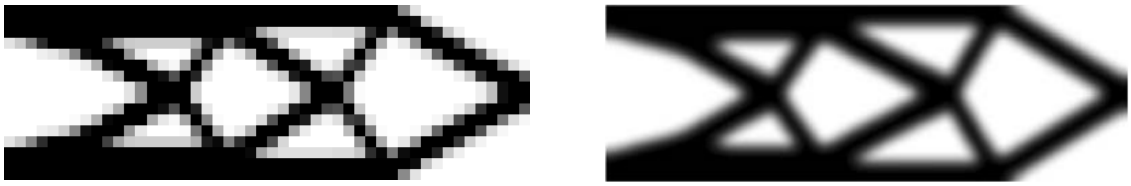

(a) (b)

Figure 2.10. 2D cantilever beam solutions (mesh size: 48×12):
(a) element based topology optimization (Q4)
(b) Multiresolution topology optimization (Q4/n25)

Element based topology optimization can generate solutions with higher resolution only when the design domain is discretized densely. This often makes the problem computationally expensive due to larger number of elements to handle during finite element analysis. Nguyen *et al*. investigated the displacement mesh requirements in the element based topology optimization for the problem in Figure 2.9 that would give comparable solution resolution with multiresolution topology optimization utilizing 48×12 elements (Figure 2.10. b). It was found that the solution resolution becomes analogous to that from multiresolution topology optimization when the design domain is discretized five time densely in each principal direction (240×60 elements) [29].

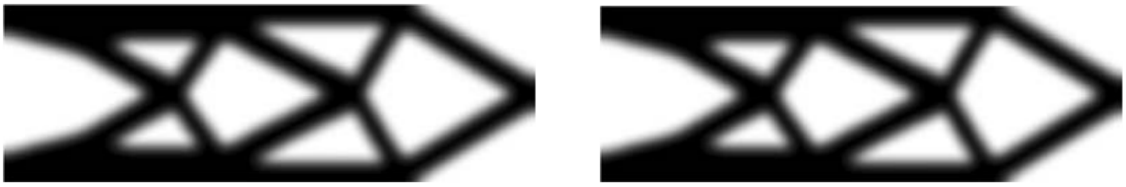

(a) (b)

Figure 2.11. 2D cantilever beam solutions with the same resolution:
(a) element based topology optimization (Q4, mesh size: 240×60)
(b) Multiresolution topology optimization (Q4/N25, mesh size: 48×12) [29]

The multiresolution topology optimization scheme is expanded to be applicable to 3D problems. Following 3D cantilever beam problem is introduced. Selected parameters include 5% volume fraction (V_s), filter size (r_{min}) of 5, and penalization power (p) of 3 are implemented.

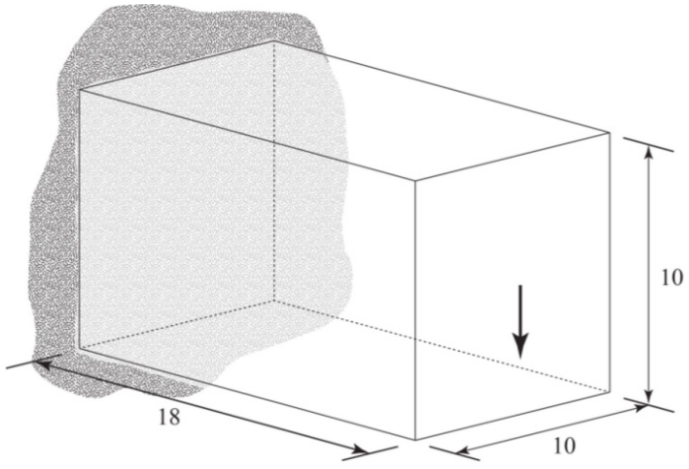

Figure 2.12. 3D cantilever beam problem

The multiresolution topology optimization solution of 3D cantilever beam problem shown in Figure 2.12 is presented in Figure 2.13. Density value of 0.25 is chosen for isosurface construction.

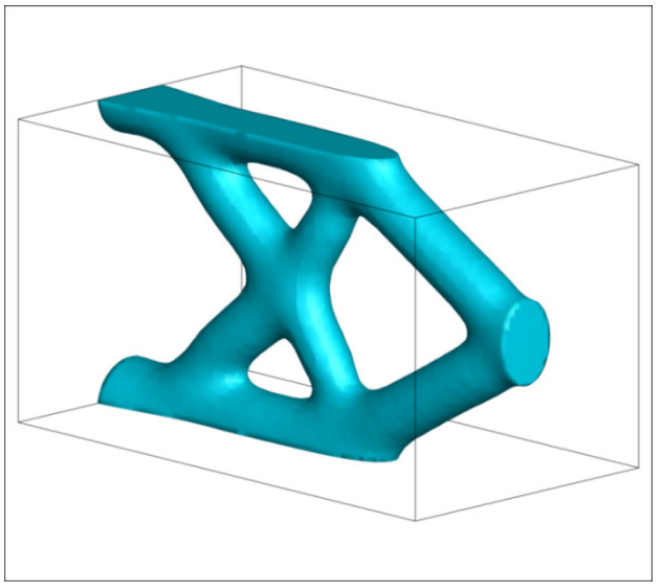

Figure 2.13. MTOP solution to 3D cantilever beam problem (ρ=0.25)

Domain and boundary conditions are modified in the second cantilever beam problem. The load is distributed horizontally along the center on the right surface. The length of one axis is reduced to 5 such that whole design domain 900 elements as shown in Figure 2.14. A volume fraction (V_s) of 15%, filter size (r_{min}) of 5, and 3 for penalization power (p) are chosen for this problem.

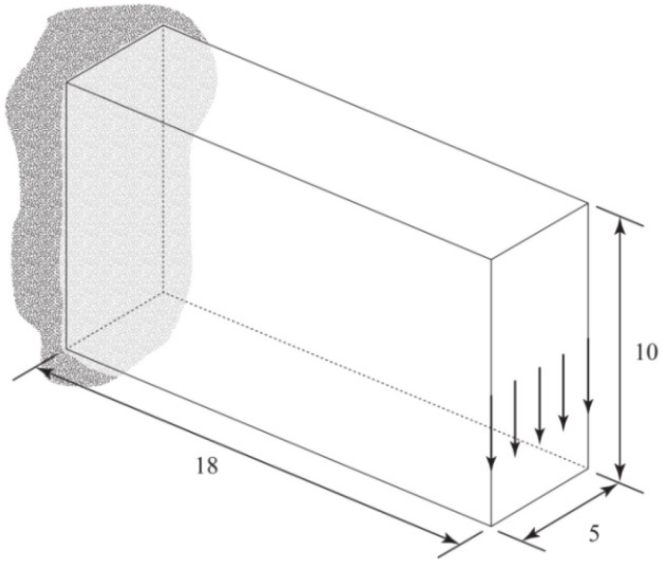

Figure 2.14. 3D cantilever beam problem II

Multiresolution topology optimization algorithm proposed the topology shown in Figure 2.15 as the solution of the second cantilever beam problem.

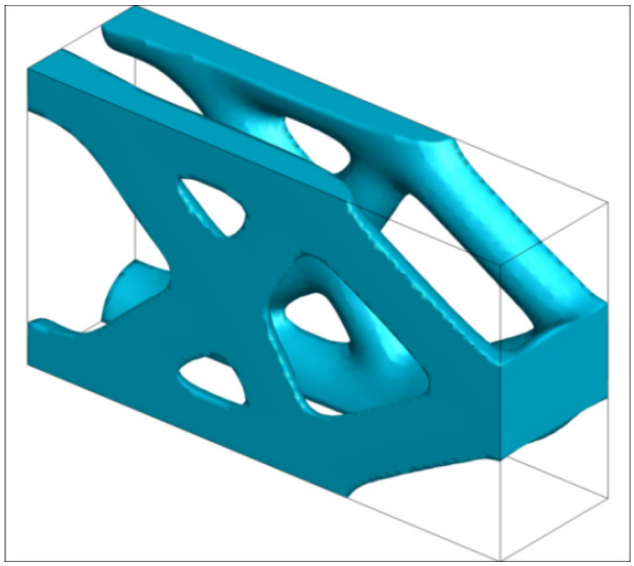

Figure 2.15. MTOP solution to 3D cantilever beam problem II (ρ=0.25)

Another 3D numerical involves the design of trestle. The problem is to design a simple vertical load bearing trestle with four areas of contact with ground. Four nodes in the center of top surface are chosen for load application. Also, total of 16 nodes at the bottom surface are fixed to represent the support condition. The design domain is cubic with 15 elements on each side totaling 3375 elements as shown in Figure 2.16.

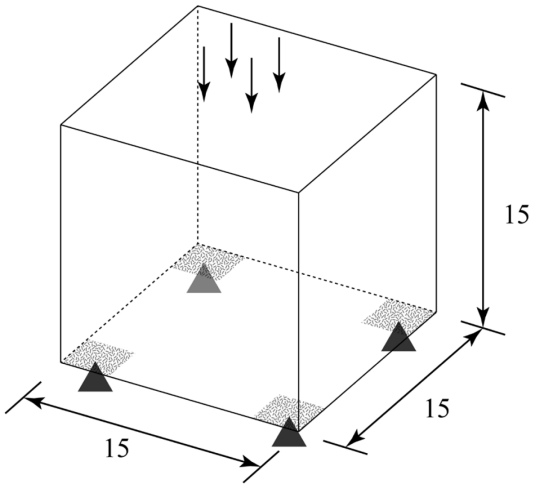

Figure 2.16. Vertical load bearing trestle problem

The solution is obtained with design parameters; volume fraction of 15%, filter size of 5, and penalization power of 3. Multiresolution topology optimization solution is shown in Figure 2.17. Density value of 0.25 is chosen for isosurface.

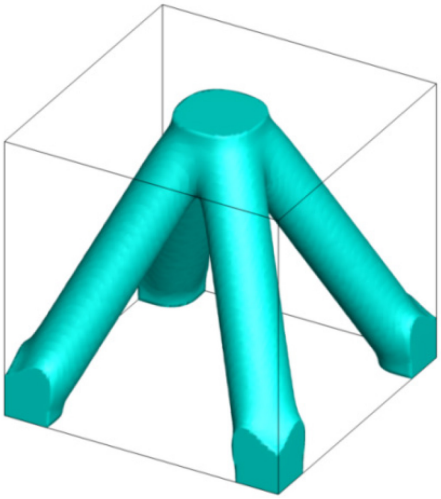

Figure 2.17. MTOP solution to vertical load bearing trestle problem (ρ=0.25)

The boundary condition used in trestle problem is applicable to many commercial design problems. In fact, the topology shown in Figure 2.17 can be found in numerous products such as car jack stands or furniture foundation as presented in Figure 2.18.

Figure 2.18. Commercial products with trestle

2.4 Summary

In this chapter, the basic formulation of element based topology optimization is reviewed. Topology optimization can propose numerical instabilities such as checkerboard pattern and mesh independencies. These issues can be circumvented with introduction of filters. Still, this element based topology optimization is not preferred in large scale problems due to demand in powerful computing source. Nguyen *et al*. proposed multiresolution topology optimization scheme that uses multiple meshes (coarse mesh for finite element analysis and fine mesh for design and density variables) which enables to obtain results with relatively fine resolution without requiring large scale finite element analysis. 2D and 3D numerical examples are shown using multiresolution topology optimization scheme.

Chapter 3 Optimized Design of Bone Replacement Shapes for Craniofacial Reconstructive Surgery

In this chapter, multiresolution topology optimization algorithm is applied to craniofacial reconstructive surgery to acquire optimal patient specific implant topology. First of all, anatomy and buttress system of human facial bones are reviewed. Then, several real patients' data are chosen and their respective topology optimized solutions by multiresolution topology optimization are obtained. Also, the effects of in-design parameters of topology optimization are discussed.

3.1 Introduction

Human facial skeleton consists of bones that are small, delicate, and prone to infection due to nearby nasal passageway, ocular globe, and oral cavity. In addition, they play an important role in securing soft tissues inside and shaping facial contour of each individual. From a mechanical point of view, as a structure in whole they do have limits in terms of properties, so it may experience deformation or fracture under extreme impacts or mechanical loadings. For instance, blast injuries can destroy portions of the facial skeleton. Also, facial skeleton experiences deformity because of unavoidable surgeries for trauma or tumor removal. These disturbances in facial skeleton require reconstruction of the structure to restore normal functions but it remains a challenging

problem for reconstructive surgeons. An inherent difference exists between defects that are sustained from accidents or cancer ablation and those that result from trauma but they are difficult in general to manage surgically because of the significant functional and aesthetic roles of the midface [35]. Reconstruction surgery not only must obliterate the defect to secure the volume for treatment but it also needs to address the issues of swallowing and nutrition, orbital function and vision, mastication and speech, and restoration of facial contour and self-image [36]. Large segmental bone defects of the midface typically require bone grafts for a successful outcome and advances in microvascular free flaps have greatly increased reconstructive options. The most commonly used composite flaps include the osteocutaneous radial forearm fibula (Figure 1.3), iliac crest, and the subscapular system of flaps [37]. The surgical planning of osteotomies has been made easier through the advent and use of virtual surgical planning, stereolithography modeling and simulation, and prefabricated osteotomy bone cutting templates [38-40]**.** However, the issues revolving around vascularity, volume and skeletal support [41], bone stock for osseointegrated implants [42, 43], and maintenance of shape and reduced bone reabsorption still pose challenges, and a lack of consensus in the optimal surgical management of maxillectomy defects remains and thus the outcome varies qualitatively case by case.

3.2 Structural System of Facial Skeleton

The primary bones of the facial skeleton include the frontal bone, ethmoid, vomer, and mandible located down the midline and the zygomatic, maxillary, palatine, and nasal bones appearing bilaterally. The frontal bone constitutes the upper face, the

zygomatic, maxilla, palatine, and nasal bones constitute the middle or midface, and the mandible the lower face. The performance of important basic life functions such as vision, speech, mastication, swallowing, and breathing depend on the integrity of these bones, as does a person's individual, unique appearance. Reconstruction of the facial skeleton is thus particularly challenging because the bones of the face have significant functional and aesthetic considerations.

The midface is responsible for maintaining a patent nasal passageway, supporting the ocular globe, and withstanding the forces of mastication. These forces are transmitted through structural pillars or buttresses within the facial skeleton [44, 45]. There are three primary vertical buttresses in the face, two anterior and one posterior, which have been well described [44, 46-49]. They are the nasomaxillary buttress, the zygomaticomaxillary buttress, and the pterygomaxillary buttress which often abbreviated as NMB, ZMB, and PMB respectively in the literature. Referring to Figure 3.1, the NMB or medial anterior buttress extends from the anterior maxillary alveolus along the pyriform aperture to the frontal process of the maxilla. The ZMB or lateral anterior buttress extends from the premolar and molar regions along the zygomaticomaxillary suture through the zygomatic arch laterally and along the lateral inferior orbital rim to the frontal process of the zygomatic bone superiorly. The PMB or posterior buttress extends posteriorly from the maxillary alveolus to the pterygoid plate of the sphenoid bone [46, 47, 49]. These buttresses create facial height and maintain the correct anatomical position of the maxilla in relation to the cranial base above and mandible below.

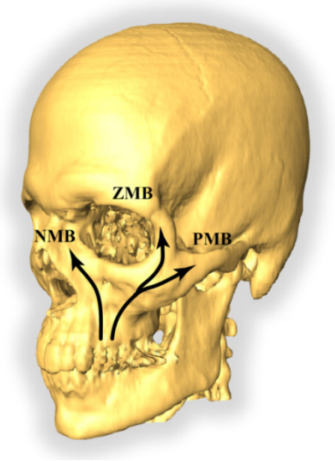

Figure 3.1. Buttress system in a human skull

The role of buttress reconstruction in relieving stress on the facial skeleton has been shown to be critical after maxillectomy in order for the facial skeleton to withstand the strong forces of mastication and other basic functional requirements [47, 50, 51]. Reconstruction of missing buttresses also makes it possible for the face to maintain its vertical height and horizontal projection.

3.3 Patient Data

Patient data with four different midface defects are shown in Figure 3.2.

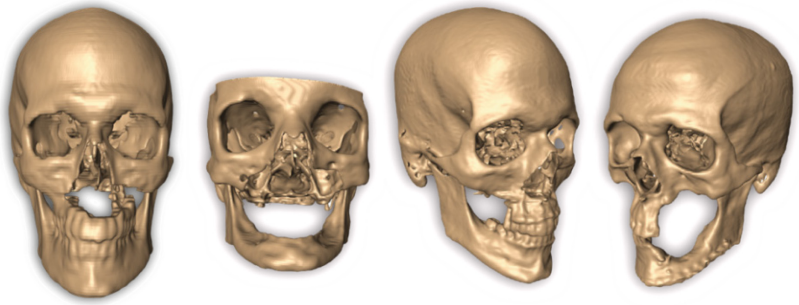

(a) (b) (c) (d)

Figure 3.2. Craniofacial skeletons of patient with severe midface defects

Bilateral maxillectomies are performed for case (a) and (b) in Figure 3.2 and comparing the image with normal buttress system shown in Figure 3.1, one can conclude that respective individuals lost the buttress systems which leads to normal activities such as appropriate mastication and speech are nearly impossible. The situations of case (c) and (d) are better as the NMBs are still intact with maxilla. The defects hinder suffering individual to maintain normal activities. Deformities shown above require reconstructive surgery in order to relieve the effect of defect and enhance the quality of living in the long run. Such reconstructive surgery needs to close the wound and separate the oral nasal cavities and retain sufficient structural support so that patients can expect normal function of facial skeleton. However, the method of using autologous tissues, not only depends on each surgeon's expertise but also is not adequate to restore appropriate load transfer mechanism in the midface. Topology optimization, introduced in Chapter 2 can be considered as a good method since its ability to propose optimum layout of the bone replacements.

3.4 Topology Optimized Patient Specific Bone Implants

Topology optimization starts with a domain of a rectangle for 2D and a rectangular parallelepiped for 3D. The domain is discretized into smaller elements by the user so that computer can calculate the material distribution in each element based on its reaction sensitivity corresponding to prescribed boundary conditions. Thus, choosing the right size of the domain is one of the most critical aspects in the technique. Multiresolution topology optimization scheme does not carry any length unit; ratios of lengths in principal directions are considered. Getting the proper domain size for craniofacial defect starts with Computed Tomography (CT) or Magnetic Resonance

Image (MRI) of the patient. The commercial software Amira (VSG - Visualization Sciences Group) [52] is utilized to read the DICOM data onto the computer screen. Appropriate threshold allows building isosurface by register skull from whole data then the data is truncated such that the data only has skull and mandible including the region of interest i.e. defect. The purpose of this step is that it tremendously reduces calculation time which leads to smoother operation in further manipulation of the image data. Once the data is truncated, one can use 2D or 3D measure tool to measure the height, thickness and the length of the region to be analyzed. The domain is selected by the surgeon because the size of defect itself only is usually not feasible domain for analysis considering later insertion and fixation i.e. pre-osteotomy could be required for better implementation of the solution.

The other important input to MTOP scheme is the load and boundary conditions. This includes information on where the loads, supports and cavities are located. Since the solution of topology optimization tremendously depend upon the boundary conditions, deciding appropriate locations of the supports and ratio of loads are essential. Once the domain size is defined, one can specify where any supports are located by using measuring tool available in any CAD or image processing software. Also, desired cavity such as nasal passageway, eye cavity or hard palate can be included.

Taking case (a) in Figure 3.2 as the model for describing the methodology of the study, domain size of each defect is measured from segmented MRI/CT scans. Using parallel perspective and 2D measurement tool, the domain size (axis ratio) of case (a) is selected as $28 \times 20 \times 12$ (width, height and depth respectively). Additional boundary conditions include, static forces on the nodes along the teeth profile representing

mastication (chewing), downward force on top surface to ensure revival of the NMB, and the supports on either lateral surfaces for contact and fixation between the implant and intact portion of facial skeleton. The load ratio between the mastication and the downward force on top surface is 0.1 and they are chosen to be purely vertical i.e. parallel to z axis. The boundary conditions in the domain are illustrated in Figure 3.3.

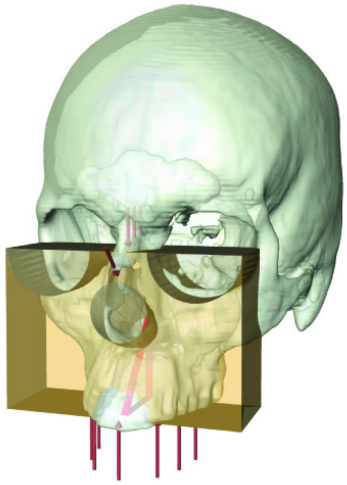

Figure 3.3. Boundary and cavity conditions for case (a)

Based on conditions in Figure 3.3, a domain with 28×20×12 (total of 6720) B8/n125 elements are introduced into the multiresolution topology optimization algorithm. Other design parameters including 12% volume fraction (V_s) constraint, penalization power (p) of 3, and filter size (r_{min}) of 5 are implemented. A PC equipped with Core i7 3.4GHz and 8GB of ram took approximately 20 seconds for each iteration. The compliance showed rapid convergence as shown in Figure 3.4 which verifies the robustness of the algorithm and validity of input conditions.

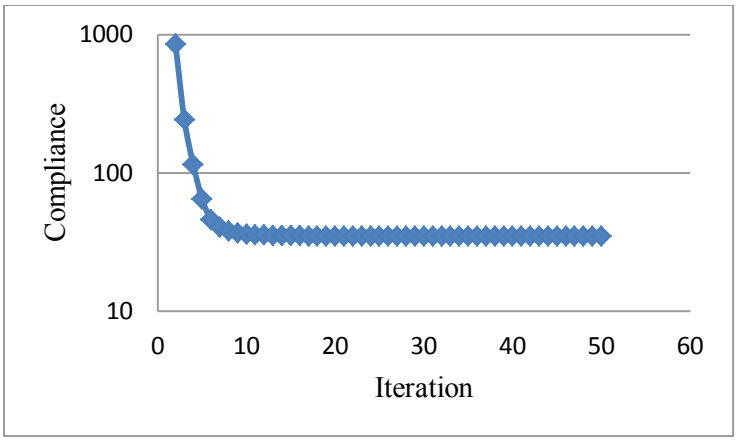

Figure 3.4. Compliance convergence history for case (a)

Final solution of MTOP scheme is exported as .DAT file for Tecplot (Tecplot, inc.) [53] for visualization. The isosurface with the density value of 0.25 of the solution obtained herein is shown in Figure 3.5. Quick visual inspection confirms that the proposed voids (nasal passageway, eye cavities, and hard palate) are well incorporated in the solution. Then, the solution was inserted to the defect (Figure 3.6) to visually verify the feasibility of final configuration.

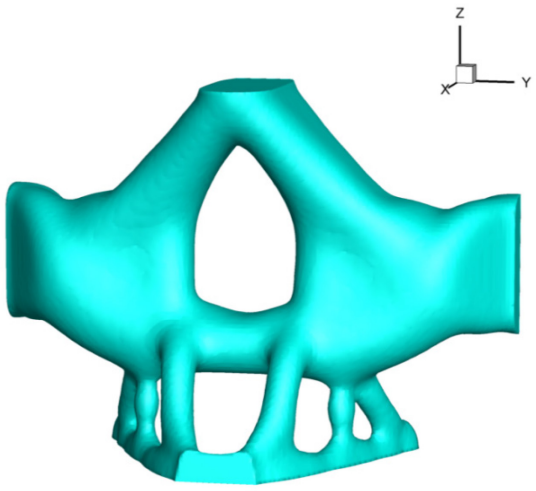

Figure 3.5. Isosurface representing the topology optimized solution for case (a) (ρ=0.25)

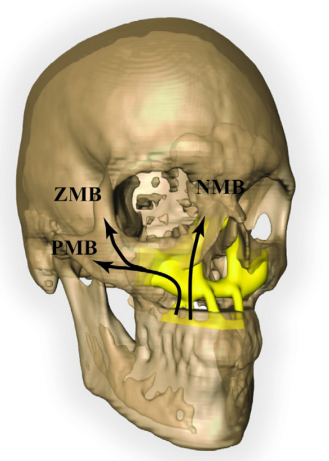

Figure 3.6. Topology optimized solution inserted into case (a)

One can see that broken buttress systems are restored when the topology optimized solution is inserted in the region of missing bone.

Same methodology was applied to obtain optimized topology of implants in remaining three cases (case b, case c, and case d in Figure 3.2). Respective design parameters (domain size, volume fraction, penalization power, and filter size) are all tabulated in Table 3.1. Also, locations of the load, support and cavities for each defect are compiled in Table 3.2. Note that grey, red, yellow, and blue in Table 3.2 represent domain, support, cavity, and load respectively.

Table 3.1. Input parameters for case (b), (c) and (d)

Case	Domain (W×H×D)	Volume fraction, V_s (%)	Penalization power (p)	Filter size
(b) – 1	32×11×25	10	3	5
(b) – 2	32×11×20	10	3	5
(c)	6×9×17	10	3	5
(d) – top	15×7×18	5	3	5
(d) – bottom	12×7×15	5	3	5

Table 3.2. Boundary conditions for case (b), (c) and (d)

Case	MRI/CT Data	Boundary conditions	
(b)	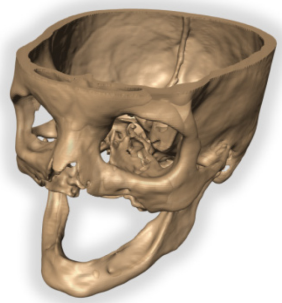	1	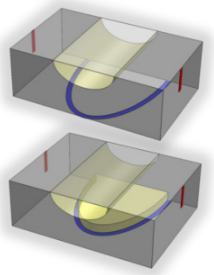
		2	
(c)		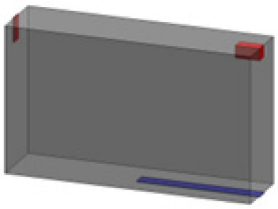	
(d)		Top	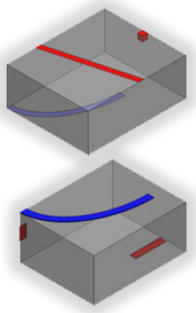
		Bottom	

Loading conditions for case (b), (c) and (d) are simpler than that of case a as they have only one load profile. Vertical are applied to these cases. However, in order to observe the effect of shear, a small amount of horizontal forces in lengthwise (y) direction is applied to case (b)-1. The load ratio of vertical direction to lengthwise

direction is chosen to be 5. Obtained topology optimized solutions were then inserted into the defect. Illustrations of final configurations are shown in Table 3.3 below.

Table 3.3. Topology optimized solutions and insertion for case (b), (c) and (d)

Case	MRI/CT Data	Results		Final Configuration
(b)	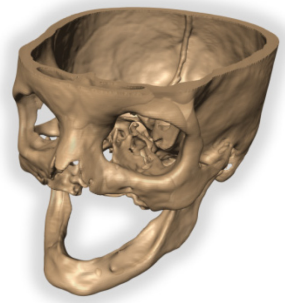	1	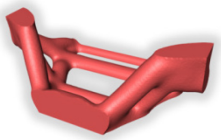	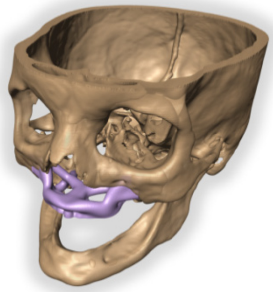
		2		
(c)	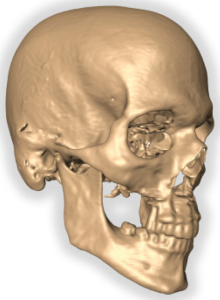	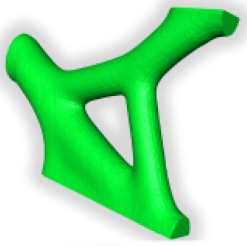		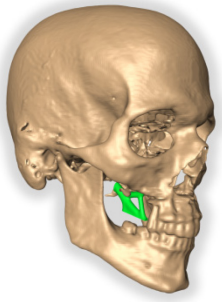
(d)		t	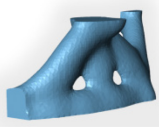	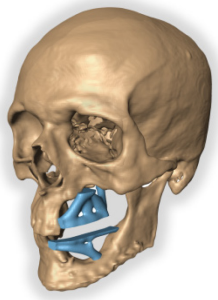
		b	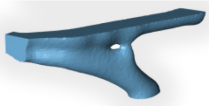	

Comparing the topology optimized solutions for case (b)-1 and (b)-2, it can be clearly seen that y shaped truss like shape at the top in (b)-2 represents the introduction of

horizontal force is well taken care of. Also, each solution not only fills the region of defect efficiently but also renovates the buttress system that may transfer the stress caused by forces to the uninjured portions of facial skeleton successfully. Accordingly, topology optimized solutions can be considered as a viable solution that fulfills the drawbacks of using surgeon dependent heuristic bone replacement shapes from autologous tissues.

3.5 Parametric Study

Resembling the nature of other structural optimization methods, topology optimization strongly depends upon design parameters such as domain size and boundary conditions. Deviation in input conditions such as modifying load ratios or size of cavities usually result in completely different topology. Also, the way that multiresolution scheme is constructed allows user to have control in in-design parameters such as mesh, filter size, or volume fractions during computation process. Therefore, it gives the user several alternate solutions for each design problems. Here, the effects of varying design parameter are explored.

The effect of parameters can be divided into two categories; direct and indirect. Indirect parameters are the ones that can be used to fine tune the results or the increase the iteration speed whereas direct parameters affect solution directly which leads to different layout. Assuming the cavity and support location remain the same, load ratio, directions, and mesh discretization falls into direct parameters whereas volume fraction and filter size and the penalization power can be included as indirect parameters. Implant variations from parameter manipulations are shown in Table 3.4.

Table 3.4. Effects of change in design parameter

Case			Proposed Solution	Volume Fraction (+50%)	$r_{min} = 3$	$r_{min} = 7$	Penal factor (4)	Load Ratio
(a)			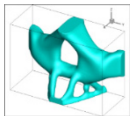	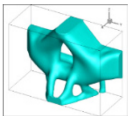	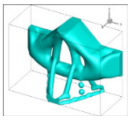	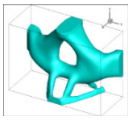	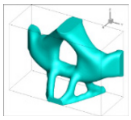	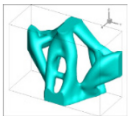
(b)	1	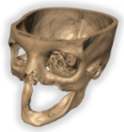	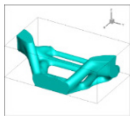	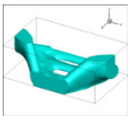	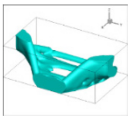	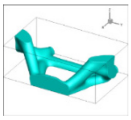	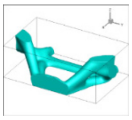	N/A
	2			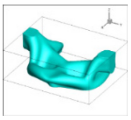	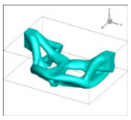	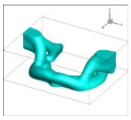	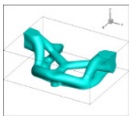	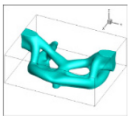
c			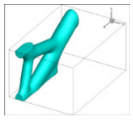	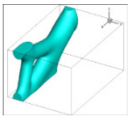	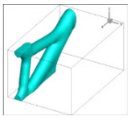	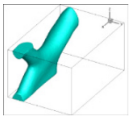	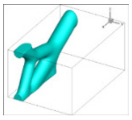	N/A
(d)	t		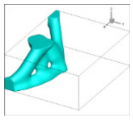	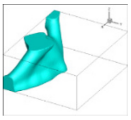	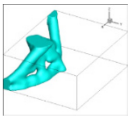	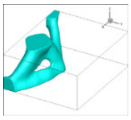	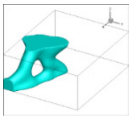	N/A
	b		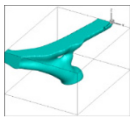	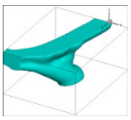	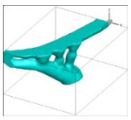	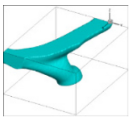	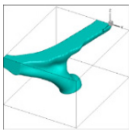	N/A

From Table 3.4, it is observed that the basic topology remains the same after altering indirect parameters i.e. volume fraction, filter size, penalization power. Thus, the effect of indirect parameters seems to be similar but they do have differences. First of all, consequences from modifying volume fraction are trivial. Relaxation on volume

constrain (V_s) allows the scheme to build thicker structure. Additionally, filter size (r_{min}) and penalization power (p) do similar things in different fashion. Essentially, large filter covers domain with bigger radius which provides more relaxed relationship between neighboring design elements. Thus, the outer surface of topology gets smoother. However, large filters are not preferred because it requires longer demand in CPU time. On the other hand, CPU time for iteration can be saved with smaller filters, but more iteration is commonly needed for convergence. Also, smooth topology is not guaranteed with small filters. Therefore, a filter size that is equal to the size of a displacement element is adequate when using MTOP scheme. As explained earlier, penalization power steers intermediate density values to converge to either 0 or 1. When bigger penalization power is employed this trend gets more pronounced as shown in Figure 3.7 and combined with a filter, this makes elements to rapidly get closer near the most critical design elements which in turn avoids abrupt changes in the final contour. Although, changing the penalization power does not change the computation time, a value close to its lower bound of 3 [7] (e.g., 3 or 4) is preferred.

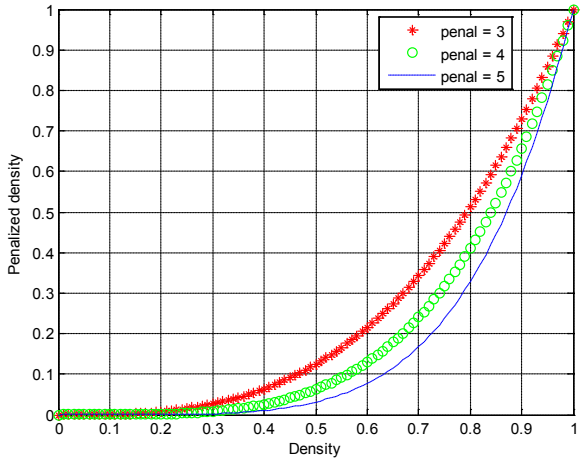

Figure 3.7. Effect of penalization power (p) on density

Changing load ratio on the other hand, often results in completely different material distribution. The effect of changing load ration from 10 to 1 is shown in Table 3.4 (case a: load ratio). Maintaining the volume fraction, significant portion of material from the top is distributed towards the bottom to endure the bigger force from mastication. In Chapter 4, proposed topology optimized implant design shown in Figure 3.5 is also validated via finite element method and mechanical testing.

3.6 Summary

In this chapter, human facial skeleton is reviewed with its components and their relationships. Fundamental engineering and aesthetic roles of human facial skeleton are introduced as well via buttress systems. However, the whole structure can be disturbed which commonly leads to failure of those buttress systems. When the buttress system fails, it needs to be restored to revive the normal living of suffering individual. Current method is not adequate to fully achieve the mission. Topology optimization method is applied to various kinds of craniofacial defect to get the patient specific shapes of bone replacements. Procedure and input parameters in applying topology optimization is discussed.

Chapter 4 Feasibility of Topology Optimized Bone Replacement Shapes

In this chapter, the bone replacement shapes using topology optimization proposed in Chapter 3 are examined to find out their mechanical characteristics and behaviors. Assuming the defect can be fully restored and bone replacement shape replaces the role of missing bones, new facial skeleton is loaded to simulate normal human mastication. Two distinct approaches including Finite Element Analysis (FEA) and mechanical testing are utilized to investigate the purpose.

4.1 Introduction

Current craniofacial reconstructive surgery for segmental bone replacements is heuristic in nature. Severe trauma, tumors are reported to be the most common midface defects which requires bone replacements [54]. Bone replacements or prosthesis needs to be patient specific. In this study, topology optimization is applied to various types of defects and respective bone replacement shapes are proposed. Although suggested shapes designed from simulations, their actual mechanical sustainability is not guaranteed after the insertion. Simulation of various conditions helps predicting its characteristics and the suitable approach to attain this would be the application of Finite Element Analysis (FEA) and appropriate mechanical testing.

In the literature, FEA has been used to widely in the field of biomedical science. Gil *et al*. utilized FEA to simulate the superelastic forming (SPF) of the maxillofacial prosthesis [55]. The simulation enabled obtaining customized patient-specific prosthesis by capturing of the thickness profile, grain size, flow stress, and strain rate during a certain pressure cycle on a given mold. Also, Kavanagh *et al*. [56] suggested using FEA in current approach for the mandible fractures i.e. Champy technique. Their work involves simulation of healthy, fractured and treated mandibles and results show that the finite element method with 3D reconstruction via medical images greatly aids the precision of the surgery and helps outcome prediction.

Although limitation exists in mechanical testing when compared to FEA in terms of analyzable data. Clelland *et al*. [57] compared the full-field strain results of splinting and non-splinting prosthesis for dental implants under load. They used Digital Image Correlation (DIC) technique to capture transient load sharing and confirmed that their result agrees with their study. Since mechanical test also has potentials for error, combination of both is recommended as one can be used as supplements to another [58].

In this work, both mechanical testing and FEA are employed to validate the result proposed in Chapter 3. The overall validation procedure is included in the work flowchart shown in Figure 4.1.

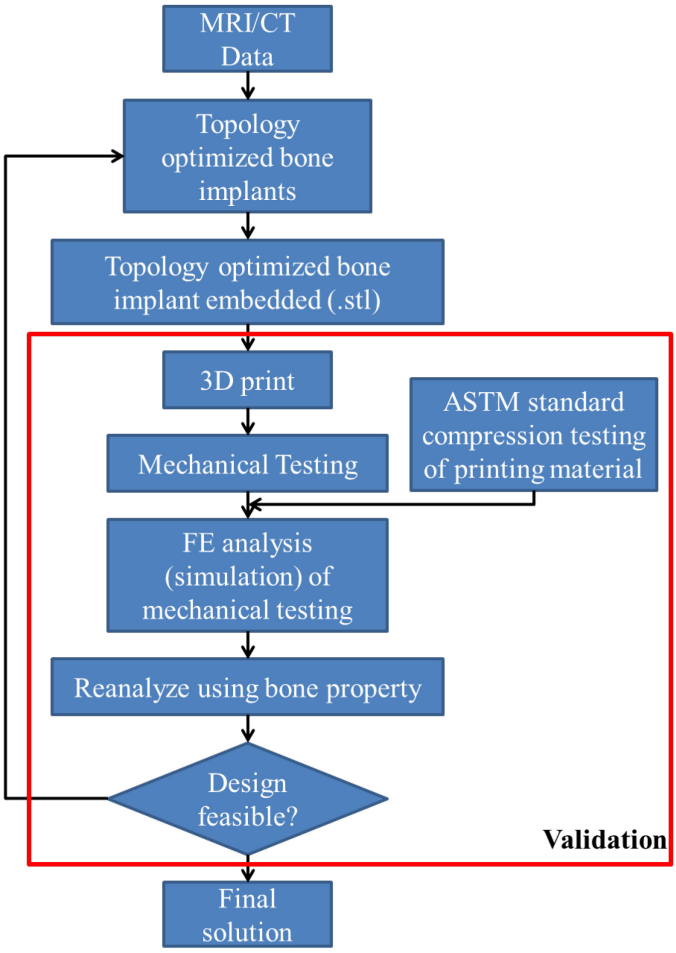

Figure 4.1. General flow of the procedure of the work

4.2 Model Preparation

Ideally, topology optimized bone replacement shapes discussed in Chapter 3 should be manufactured, positioned and fixed such that functions of facial skeleton can be recovered. Typically, surgeons use combination of plate and screws to ensure the attachment of the implant after insertion. Depending upon the size of the defect, vascularization may be necessary as well. Then, the healing starts in the forms of tissue regrowth and bone formation. As the macrostructures proposed in 0 are designed with

consideration of mechanical aspect only, this study explores mechanical behavior of the new facial after the insertion.

In order to obtain the skull with topology optimized bone implant appropriately embedded, mandible and skull needs to be separated. Dicom data of patient is manipulated through applying suitable threshold to extract the skull data. Segmentation allows extracting skull by cutting the data near upper condyles in mandible. Extracted skull surface file is converted into stereolithography (.stl) for easier manipulation. Then, topology optimized solutions needs to be positioned. Once scaling and positioning of implant onto the skull is finished, implant and skull are combined simulating insertion. If necessary, denture can be included in the combining process. The process is illustrated in Figure 4.2. Final configuration is re-meshed to alleviate the discrepancies in mesh size between components.

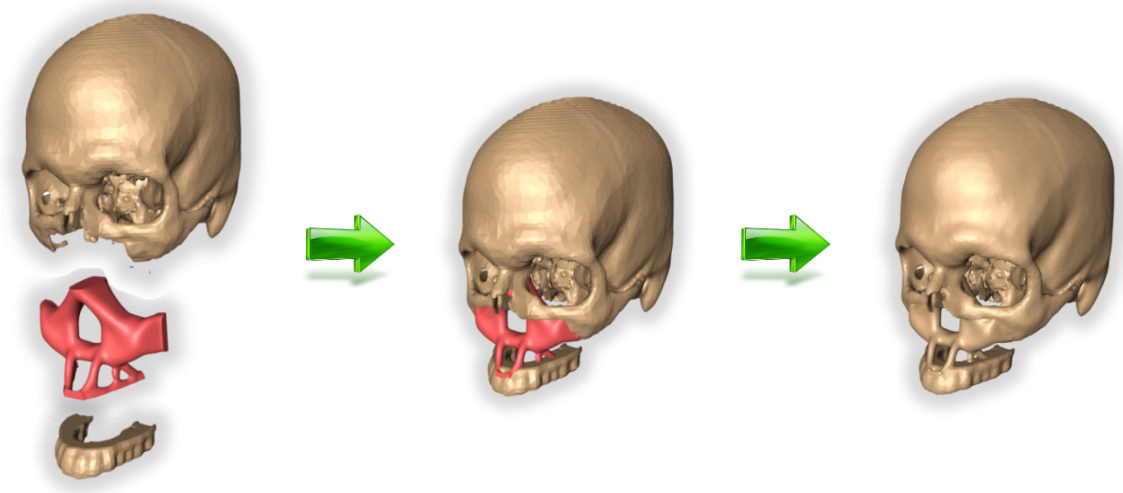

(a) (b) (c)

Figure 4.2. Embedding topology optimized solution into the skull:
(a) Components (skull, implant, and denture) (b) Assembly (c) Final configuration

Once the components are successfully combined, the outcome needs to be prepared in two different ways; polygon mesh for 3d printing, tetrahedral mesh for simulation. Amira [52], a 3D image analyzing software, is used to convert existing stereolithography with surface triangular mesh to volume tetrahedral mesh.

4.3 Mechanical Testing of the Patient Skull Model

Surgical planning plays an important role in improving the outcome quality by minimizing the chances of abrupt intraoperative issues that require surgeon's ad hoc decisions [59]. The development in clinical imaging such as Computed Tomography (CT) has tremendously helped surgeons in preoperative planning since 1987. However, for surgical planning, 3D reconstruction from the 2D CT scan images is useful because it allows surgeons to have actual models for hands-on simulation. Recent advances in 3D imaging enable to render volumetric models, and nowadays 3D printers precisely fabricates them to make the surgical simulation virtually real [60].

In this work, the stereolithography of skull model that is prepared from the Boolean addition of skull and topology optimized implants is sent to Dimension SST 1200es (Stratasys Inc.) for the mechanical testing. SST 1200es is a 3D printing hardware which follows the Fused Decomposition Modeling (FDM). Thermoplastic e.g. Polylactide (PLA) or Acrylonitrile butadiene styrene (ABS) in the form of thin wires is common material that fused decomposition modeling uses. First of all, the system scans the surface of the input model and determines the nozzle traveling path after the segmenting the model into finite number of horizontal layers. Then, thin wire is heated up to melting point and becomes even thinner while traveling through the nozzle to improve

the productivity and the resolution of outcome. The illustration of this process is shown in Figure 4.3. Also, skull model produced with fused decomposition modeling using ABS plus is presented in Figure 4.4.

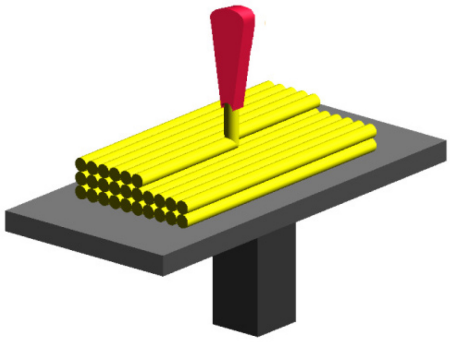

Figure 4.3. Illustration of Fused Decomposition Modeling (FDM) process [61]

Figure 4.4. Skull model fabricated with fused decomposition modeling

To explore the behavior of the skull model, simulation of human mastication is selected. Maximum human masticatory force, which is reported as 500N [62, 63], is

chosen to be applied in the one side of molar region while the skull is held stationary. Also, the testing is repeated three times to see the convergence of the result. In order to reflect abovementioned boundary conditions and loading to be applied, aluminum fixture is designed in CAD and fabricated (Figure 4.5). Then, the fixture is attached onto the XY table of Instron 1321 servo-hydraulic load frame (Instron®) to finalize the setup (Figure 4.6). Also, cylindrical load applicator made with aluminum is chosen which has a cross-sectional area similar to the area of two molar teeth. This load applicator is hinged in the middle so that the top portion is versatile to better contact with the model as shown in Figure 4.7.

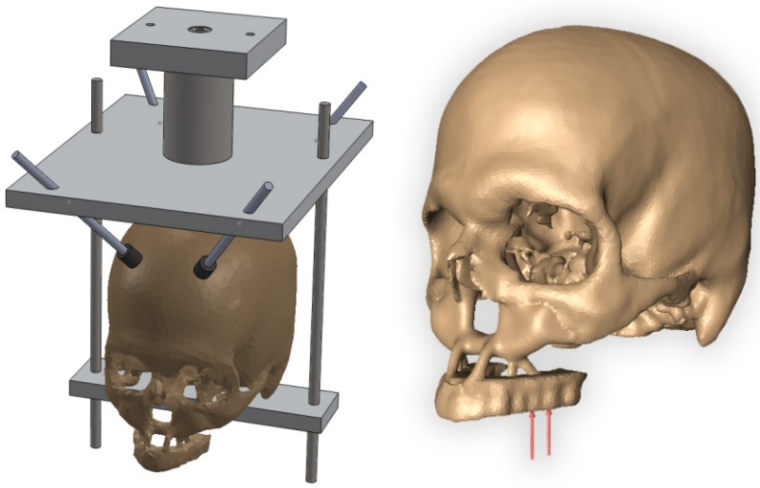

Figure 4.5. Design of skull model fixture with selected loading

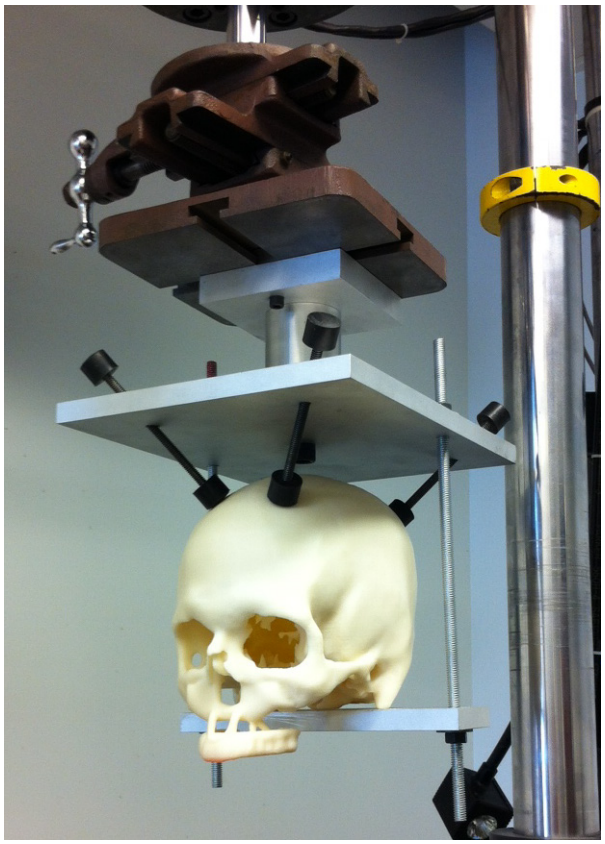

Figure 4.6. Mechanical testing setup

Figure 4.7. Load applicator

3D image correlation technique is employed to capture the behavior of the skull model under load. Commercial image correlation software Vic3D (Correlated Solutions) is used to process the image data. A pair of high resolution Grasshopper camera (Point

Grey Research, Inc.) equipped with 35mm Schneider lenses is positioned to capture strain distribution in the model. First, the surface of the model is covered with spray paint to make random dot patterns as shown in Figure 4.8. This allows cameras to stabilize data capturing during the testing.

Figure 4.8. Dot patterned skull model for enhance data capture

Two cameras are arranged to create a stereovision of the model. In this configuration, calibration of each camera takes place by taking pictures of calibration grid at various angles. These calibration pictures are used to establish common 3D coordinate systems for both cameras. While abovementioned optics gather the transient deformation of the model, a load frame controller (MTS FlexTest SE) is set to record the load and stroke history of the Instron 1321 load frame. Final configuration including skull model, fixture, load frame, load applicator, and data gathering cameras are shown in Figure 4.9.

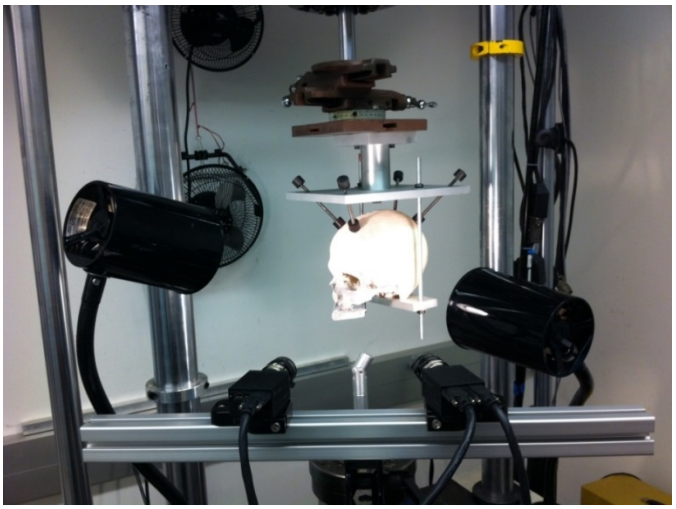

Figure 4.9. Final configuration of mechanical testing

With the given setup, the skull model aligned with load applicator such that ramp load with maximum magnitude of 534N (≅120lb) can be applied on first and second molar teeth on the right hand side of the skull model as Figure 4.10. The profile of the load and actual stroke travel is shown in Figure 4.11.

Figure 4.10. Skull position for loading at first two molar teeth

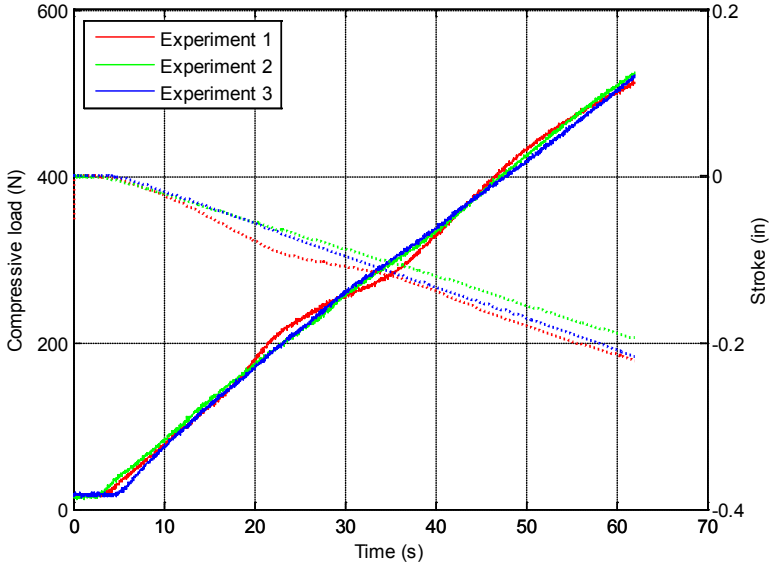

Figure 4.11. Load and stroke history for all three testing

4.4 Mechanical Testing of Fused Decomposition Modeling Material

In order to successfully replicate the mechanical testing discussed in section 4.3, the material property and boundary conditions needs to be precisely implemented. The 3D printer used to fabricate the mechanical testing model uses ABS plus. Although tensile property of ABS plus is readily available, it cannot be used in this FEA because of three reasons. First, the direction of FDM can cause anisotropy within the model. Second, heat application to melt the material before ejection through nozzle may alter the material property. Lastly, the mastication force applied in molar region makes compressive stress to dominate in the model. Appropriate mechanical testing is conducted to explore the property of ABS plus in compression. Three exactly same specimens that meet the ASTM standards (D695: Standard Test Method for Compressive Properties of Rigid

Plastics) are prepared for compression testing; geometry and dimension are shown in Figure 4.12.

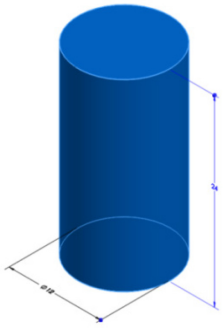

Figure 4.12. Compression testing specimen

Setup which is similar to that of mechanical testing of skull model in section 4.3 is employed for the testing. Following ASTM standards, a ramp load that will generate strain rate of 8.333E-4 is chosen till 50% strain in 600 seconds. Figure 4.13 shows the specimen deformation due to the load.

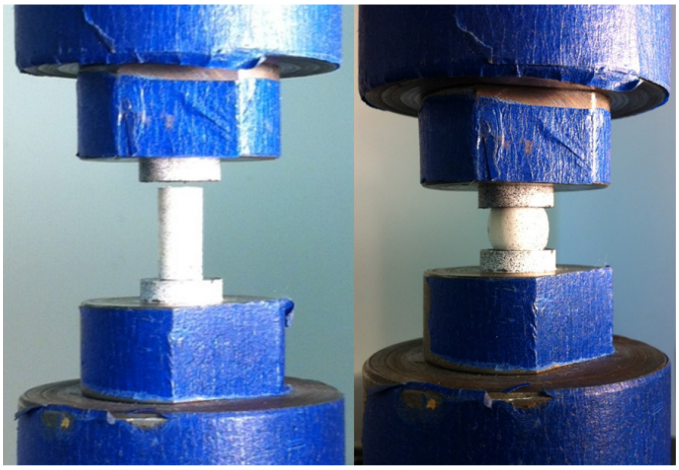

Figure 4.13. Specimen deformation under compression

The mechanical behavior of the specimen under compression is captured using image correlation technique. Engineering strain is extracted by a virtual extensometer positioned in specimen's longitudinal direction on the image (Figure 4.14). Then, stress and strain relationship is obtained by relating the strain data with the loading profile. Figure 4.15 shows the true and engineering stress strain plots. All three specimens show similar results. Experimental Young's modulus of the printing material turned out to be 2.074GPa (Figure 4.16).

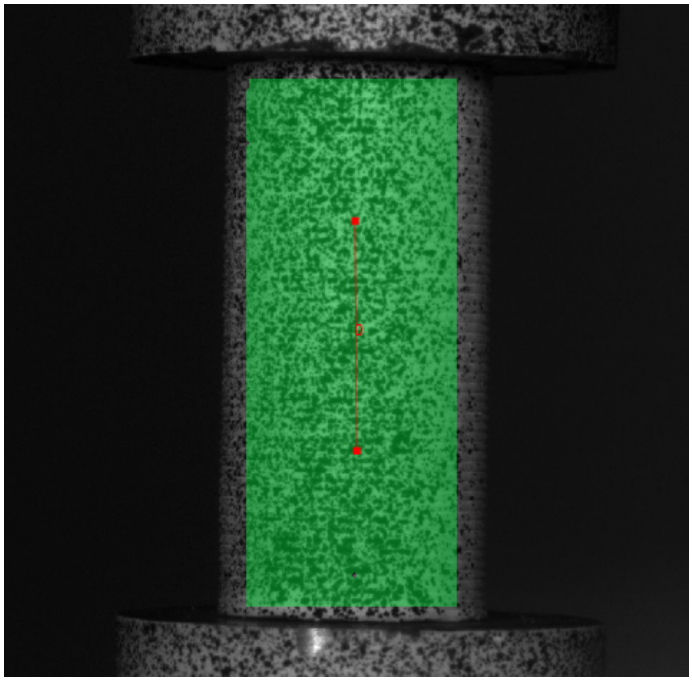

Figure 4.14. Extensometer (red) for engineering strain calculation

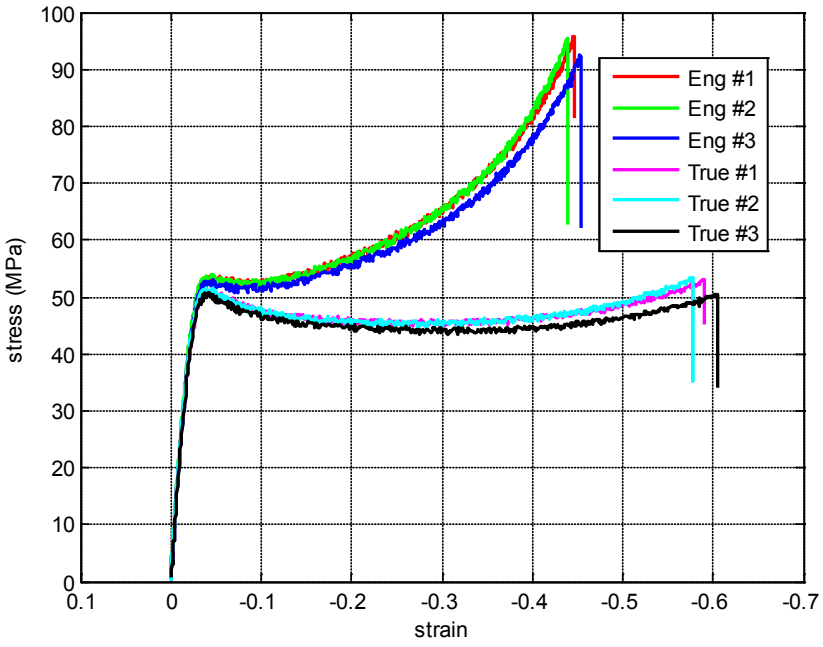

Figure 4.15. Stress strain curve of specimens under compression

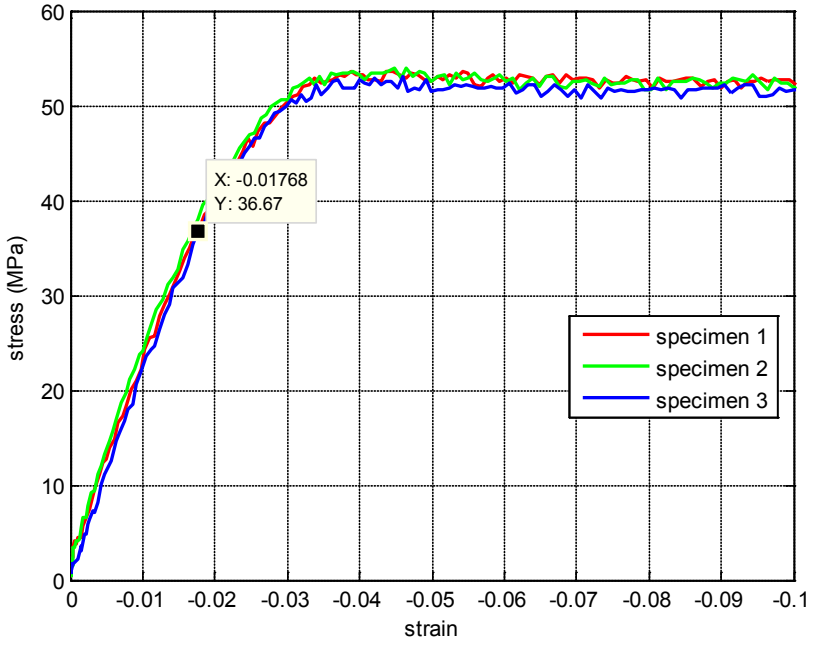

Figure 4.16. Data point used for compressive modulus

4.5 3D FE Analysis of the Patient Skull Model

Array of 2D triangular elements which represents the outer surface of the skull model underwent element conversion through Amira [52] so that the model is defined with 3D tetrahedral elements. A commercial FEA tool, ABAQUS [64], is chosen. The skull model consisted with a total of 155195 linear tetrahedral elements with 41492 nodes is shown in Figure 4.17.

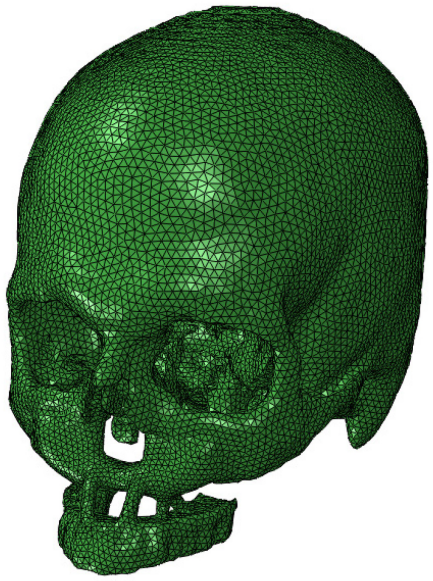

Figure 4.17. FE model of the skull model in ABAQUS

Young's modulus of 2.074GPa and material yield strength using 0.2% offset method of 53MPa are obtained from the experiment (section 4.3) is used with a Poisson's ratio of 0.35. Plastic behavior after the yielding is also taken into account in the FE model

by introducing plastic strain values into the software. Estimated material property for FEA purpose from compression testing is shown in Figure 4.18.

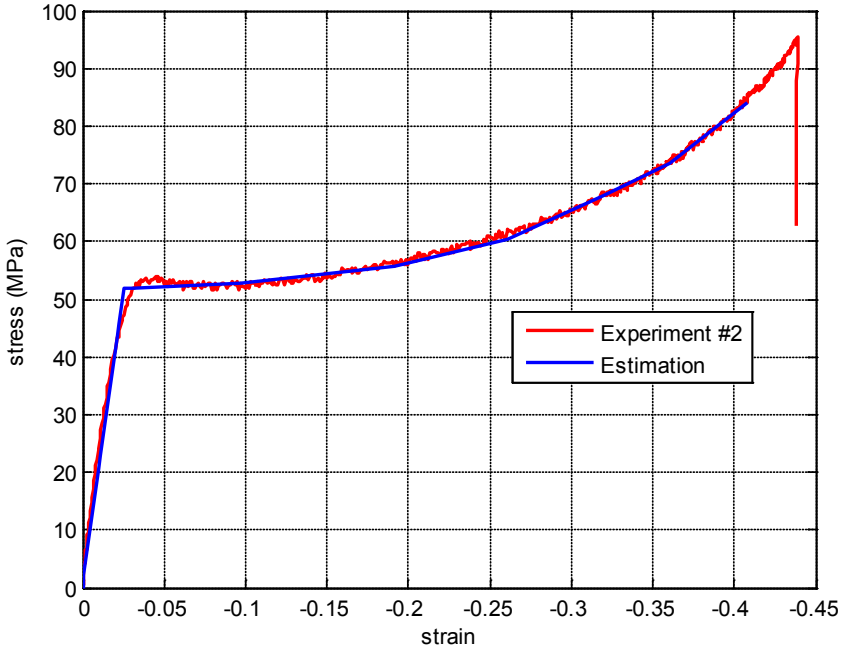

Figure 4.18. Estimated material property for finite element model

The boundary conditions to match the mechanical testing setup are employed. They include four areas in the top of skull and two areas in the bottom most portion of skull. Their movement and rotation under the load is prevented by fixing the nodes of aforementioned locations. Also, 267N which is the half of the maximum load in the mechanical testing is applied on 23 nodes in the region of first and second molar teeth as concentrated forces with magnitude of 11.61N each in vertical direction. Boundary and loading conditions are shown with that of mechanical testing in Figure 4.19.

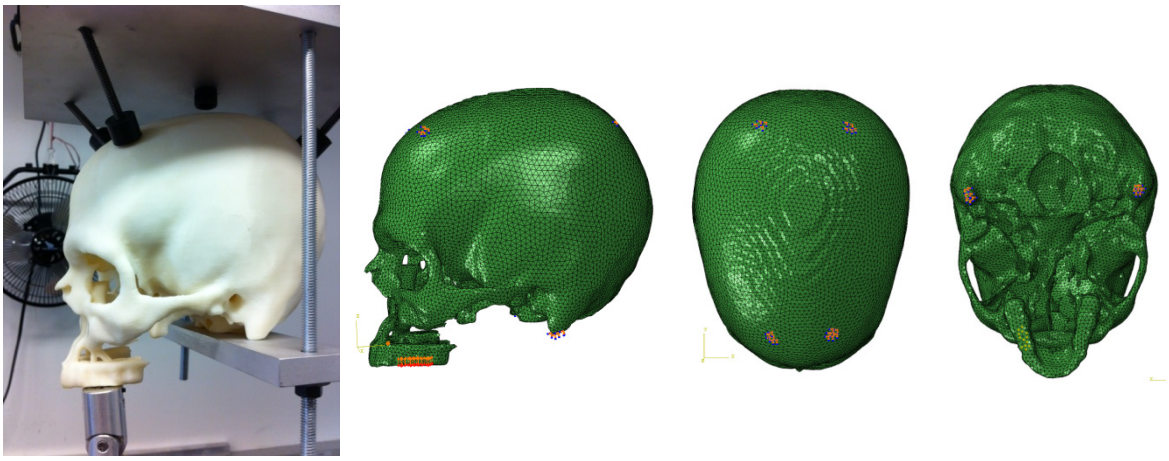

(a) (b) (c) (d)

Figure 4.19. Boundary and loading conditions: (a) Reference model (mechanical testing) (b) side view (c) top view (d) bottom view

4.6 Results and Discussion

The purpose of mechanical testing and FEA is to explore the feasibility of topology optimized solution in a situation where it has replaced the region of defect. Buttress systems in human facial skeleton are responsible for smooth transfer of stress generated by external load such as mastication. The structure also needs to withstand the maximum force subjected to an uninjured human facial skeleton. This mechanical role needs to be revived in order for topology optimized solution to be acceptable. The skull model, presented in earlier section, has several truss-like structures towards the bottom where denture is placed as depicted with rectangle in Figure 4.20. They are thin and skewed from the axis of vertical loads and thus anticipated to be the most critical region. The strain and stress distribution are examined from both mechanical testing and FEA.

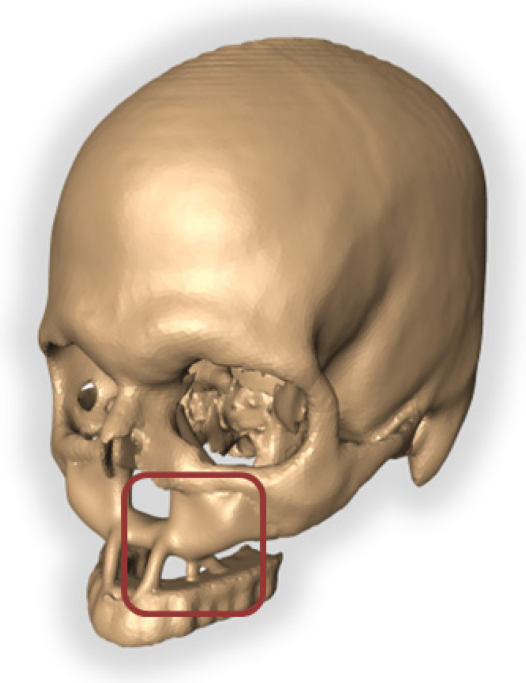

Figure 4.20. Region of interest on the skull model for analysis

The result from FEA is compared with that from the mechanical testing to test reliability of FE model. Image correlation technique employed in the mechanical testing is capable of capturing Lagrangian strain. Strains in vertical (e_{yy}: mechanical testing, E33: FEA) and horizontal (e_{xx}: mechanical testing, E11: FEA) directions in elastic region are compared between the mechanical testing and FEA. The stress and strains contour from FEA of skull model are presented in Figure 4.21. Note that contours are zoomed into region of interest depicted in Figure 4.20 for strain results (Figure 4.22 and Figure 4.23). Coordinate is transformed in the visualization module in Abaqus [64] to match that in mechanical testing. Stress contour shows the model is in elastic region. Load matching data from mechanical testing is presented in Figure 4.24 through Figure 4.29.

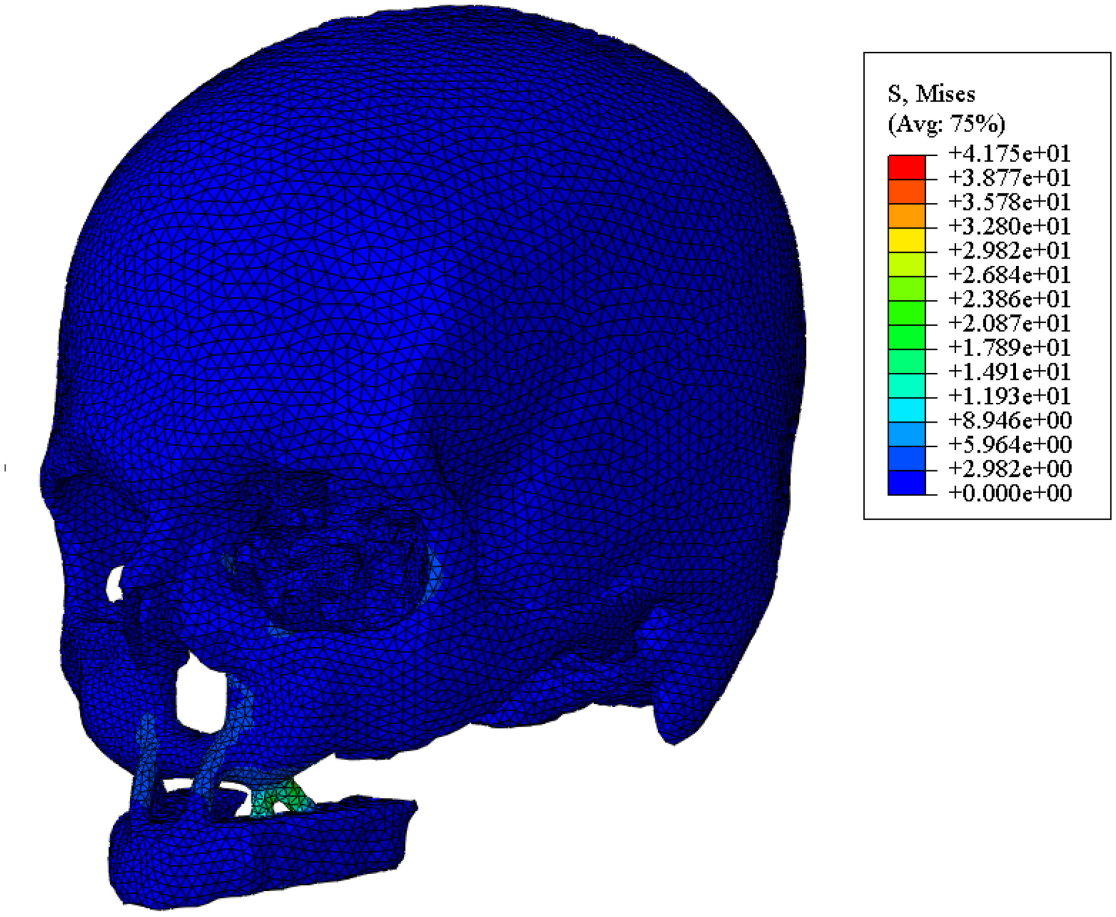

Figure 4.21. Von Mises stress contour from FEA of skull model

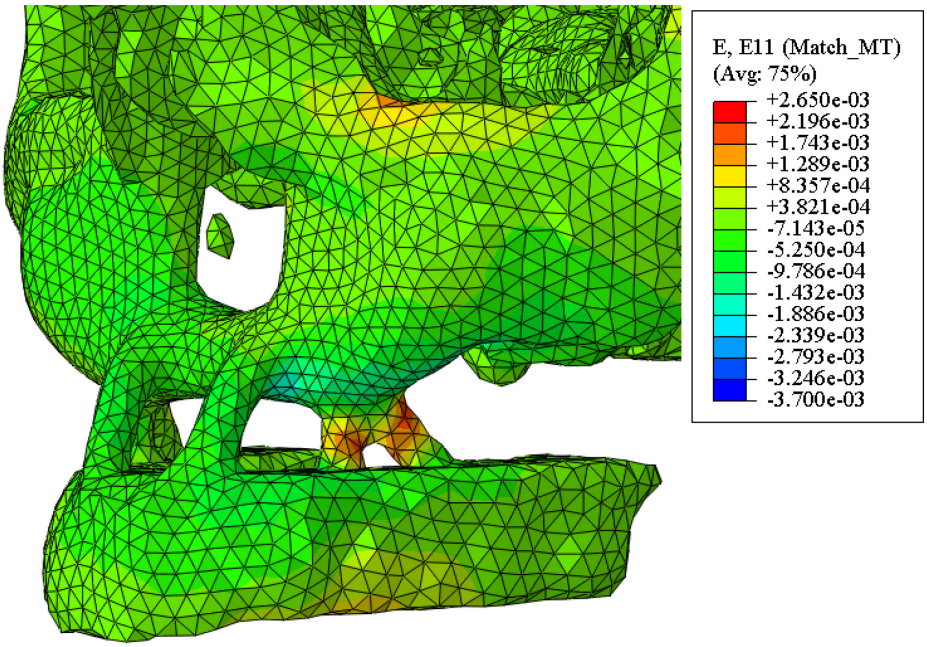

Figure 4.22. Strain contour in horizontal direction (E11) from FEA of skull model

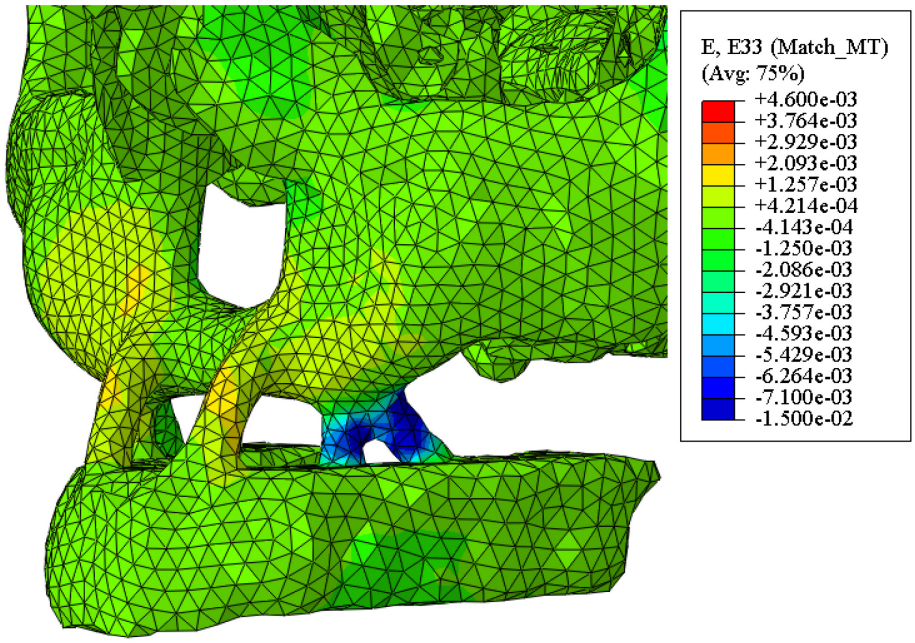

Figure 4.23. Strain contour in vertical direction (E33) from FEA of skull model

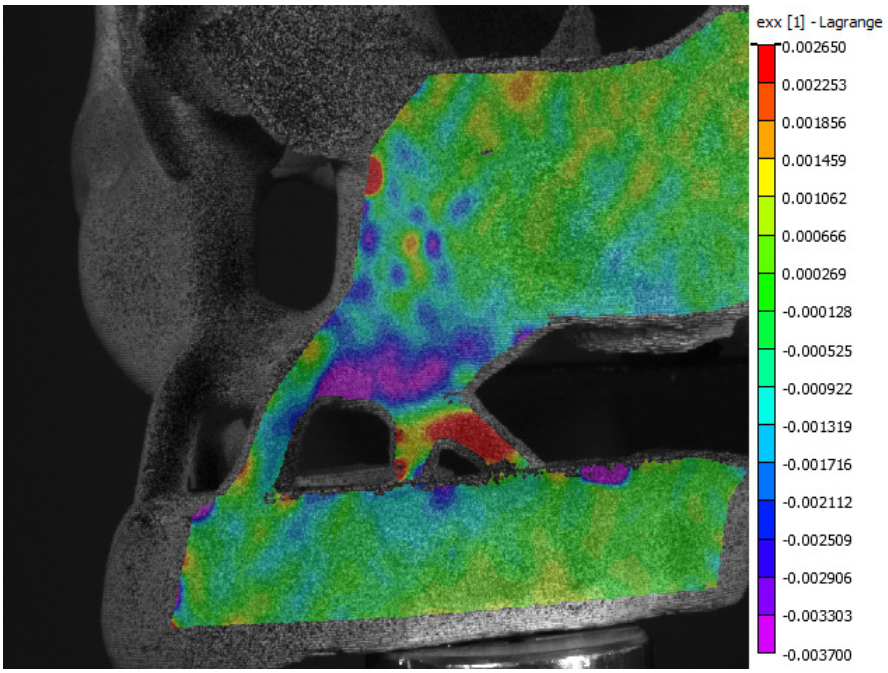

Figure 4.24. Strain contour in horizontal direction (e_{xx}) from skull mechanical testing #1

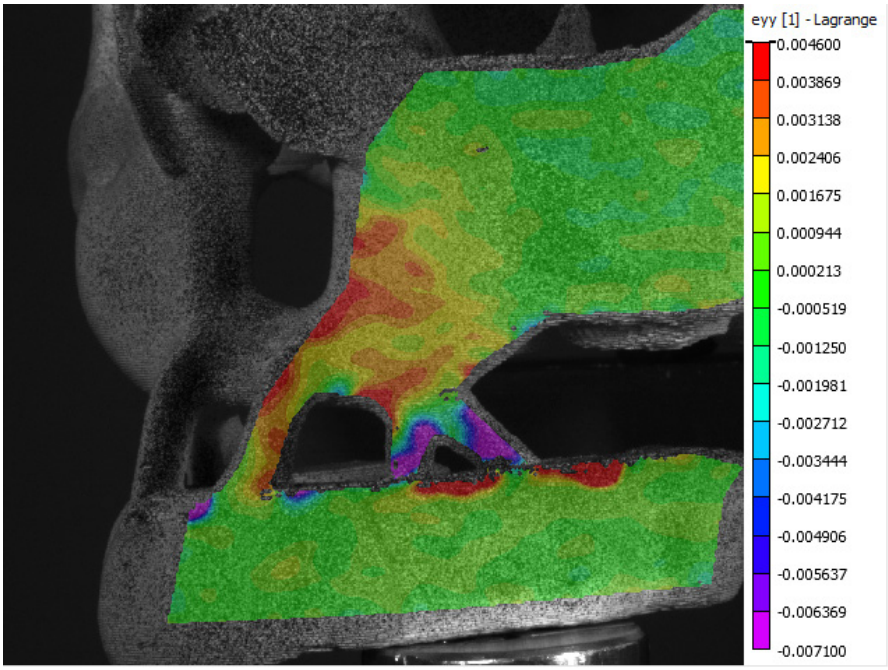

Figure 4.25. Strain contour in vertical direction (e_{yy}) from skull mechanical testing #1

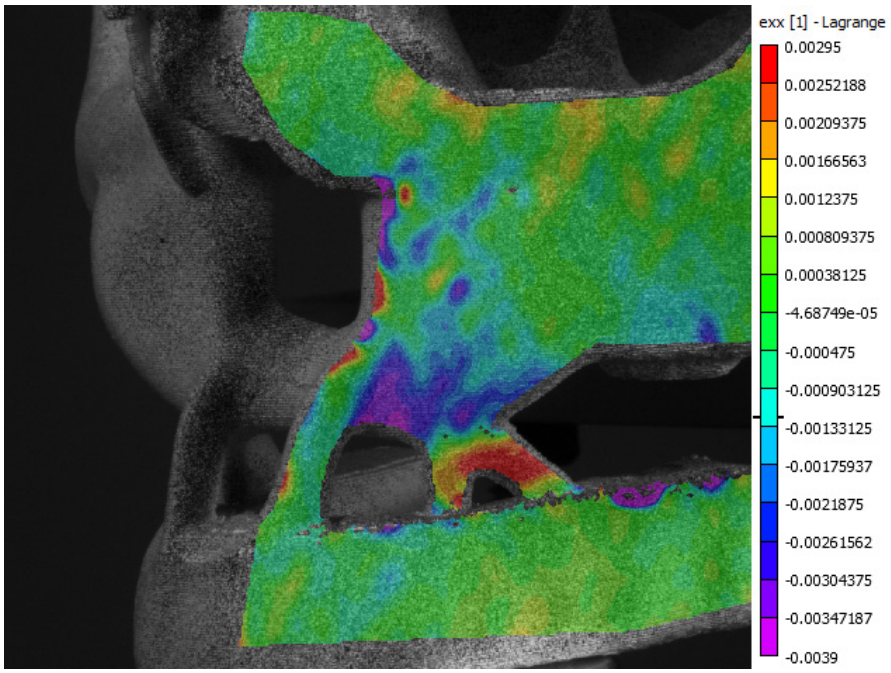

Figure 4.26. Strain contour in horizontal direction (e_{xx}) from skull mechanical testing #2

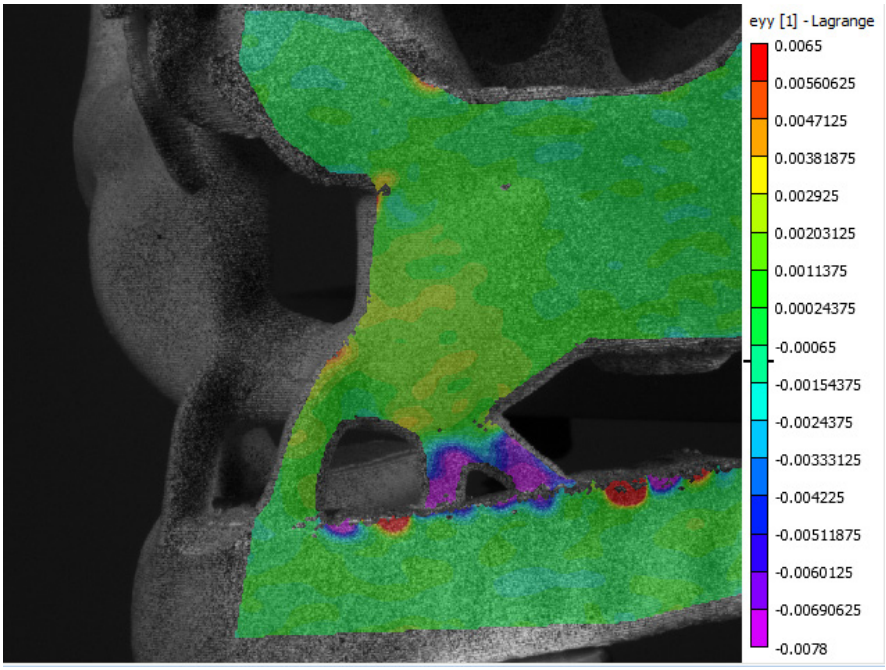

Figure 4.27. Strain contour in vertical direction (e_{yy}) from skull mechanical testing #2

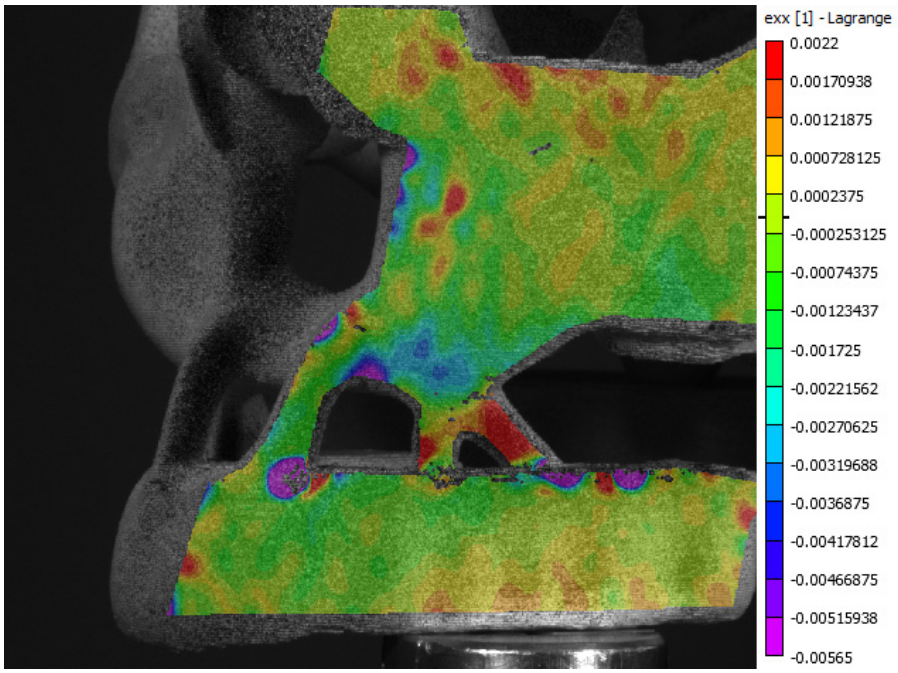

Figure 4.28. Strain contour in horizontal direction (e_{xx}) from skull mechanical testing #3

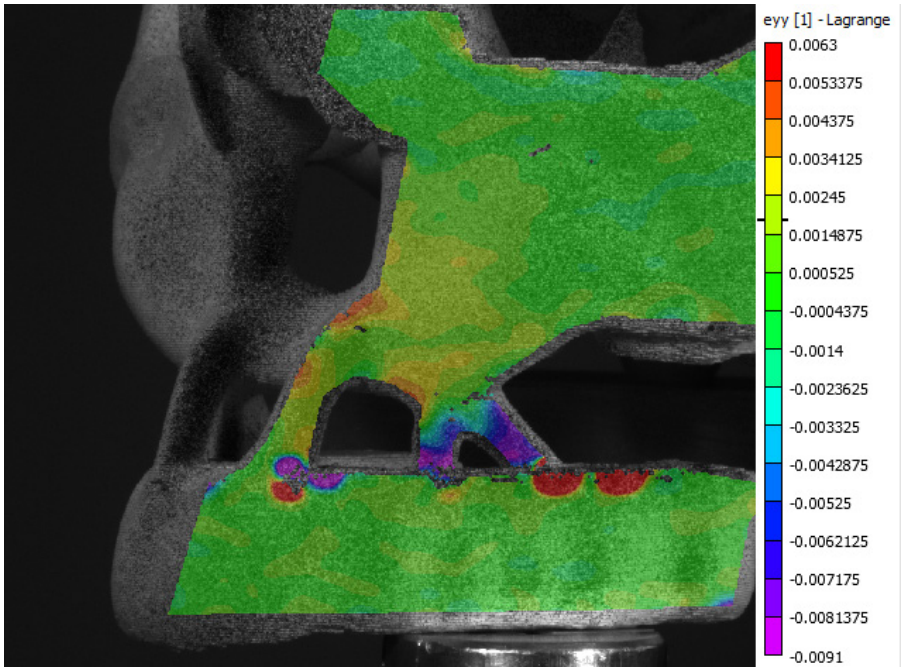

Figure 4.29. Strain contour in vertical direction (e_{yy}) from skull mechanical testing #3

Quick visual comparison shows that FEA of skull model successfully follows the strain contours from three mechanical testing qualitatively. Five elements that are located in the most critical region as shown in Figure 4.30 are selected to check the quantitative discrepancies. The percentage differences are reported in Table 4.1.

Table 4.1. Quantitative result comparison between FEA and mechanical testing: strain in vertical direction (e_{yy}: mechanical testing, E33: FEA)

Element	FEA	EXP1	EXP2	EXP3	% Difference
	E_{33}		e_{yy}		
2214	-0.0047618	-0.0048051	-0.0049072	-0.0050311	**3.21**
4512	-0.0085455	-0.0085127	-0.0086461	-0.0068741	**6.26**
2212	-0.0122200	-0.012888	-0.123581	Data loss	**3.52**
4051	-0.0079125	-0.0075546	-0.0076256	-0.0079400	**2.60**
1706	-0.0075702	-0.0075080	-0.0075213	-0.0072705	**1.81**

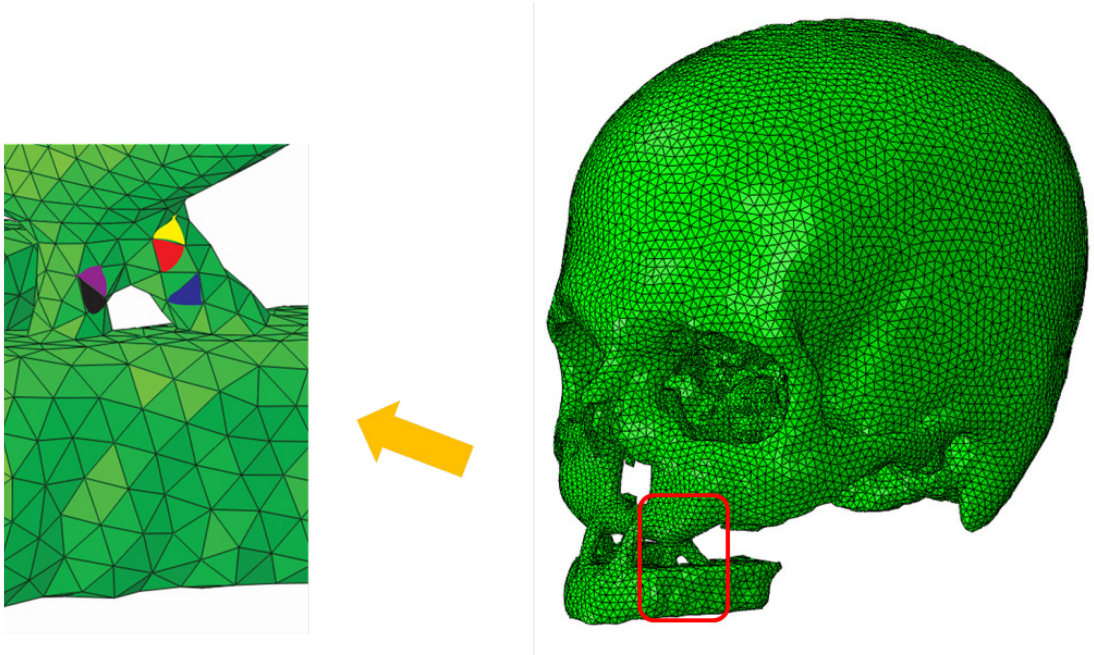

Figure 4.30. Five selected elements in skull FE model for comparison with mechanical testing results

Thus, results from FEA simulation match the mechanical testing result reasonably (6.26% maximum difference). Larger differences appear in the horizontal strain values as shown in Table 4.2. There are numerous factors that may have brought the differences. The most critical reason is that the inhomogeneity of the printed material. The way fused decomposition modeling works creates anisotropy in the printed object due to voids in the direction parallel to the printing layers as shown in Figure 4.31. Also, Poisson's ratio of 0.35 used in FEA is obtained through communication with the printing material company. Thus, if the material of skull model is purely isotropic, a closer result in horizontal direction can be expected.

Table 4.2. Quantitative result comparison between FEA and mechanical testing: strain in horizontal direction

Element	FEA	EXP1	EXP2	EXP3	% Difference
	E_{11}		e_{xx}		
2214	0.0024463	0.0026751	0.0022318	0.0021318	**4.09**
4512	0.0025962	0.0020421	0.0025015	0.0012015	**12.5**
2212	0.0026297	0.0025922	0.0023492	Data loss	**6.05**
4051	0.0021997	0.0030881	0.0027011	0.0027518	**29.4**

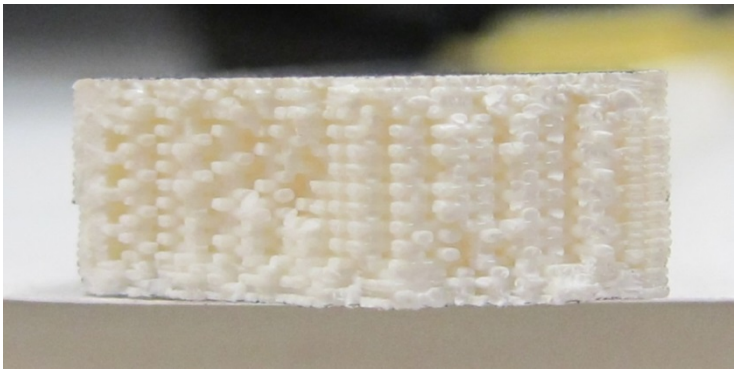

Figure 4.31. Material inhomogeneity from fused decomposition modeling

Another possible source of error is the improper alignment of the vertical load applicator. Loads are assumed to be purely vertical but the direction of loads may have deviated from vertical axis during mechanical testing preparation. Also, load bearing region is no longer perfectly smooth in skull FE model during converting 2D triangle elements in stereolithography to 3D tetrahedron elements. Evenly distributed load through cylindrical load applicator is represented as concentrated point loads in FE model. However, recognizing that compression dominates in both experiment and FEA, negligible compressive strain (e_{yy} and E33) discrepancy (2~6%) tells that FEA of skull model effectively represented the compressive behavior from mechanical testing.

A load transfer mechanism may be traced from the FEA of skull model. Directional components of stresses are plotted in the midface in Figure 4.32. The result show that significant amount of stresses are transferred through the topology optimized solution near nasal cavity (red dashed) and black solid region which resembles the role of natural load transfer mechanism i.e buttress systems.

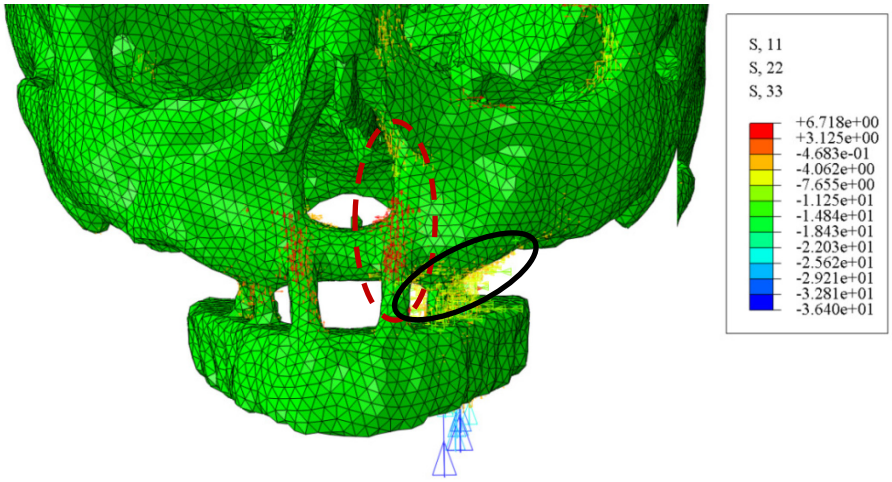

Figure 4.32. Load transfer mechanism found from the experiment

Human bone is a very complex and completely anisotropic material. While simple anatomic theory of bone exists (Stiff and dense cortical bone surrounds soft and coarse cancellous bone), obtaining mechanical property of human skeleton system is still lacking. In 1970, McElhaney *et al*. [65] examined the mechanical property of human skull . They conducted mechanical tests on human skull and concluded that the skull bone is fairly isotropic in directions tangent to the skull [65]. Experimental tangential compressive properties from their work are provided in Table 4.3.

Table 4.3. Mechanical property of human skull bone [65]

Tangential compressive property	No. of specimens	No. of donors	Mean	Standard Deviation	Skull to skull significant differences
Modulus (GPa)	219	14	5.584	3.034	Yes
Poisson's ratio	327	18	0.22	0.11	No
Ultimate strength (MPa)	210	14	96.53	35.85	No
Ultimate strain ($\times 10^{-3}$)	210	14	51	32	No

Although McElhaney *et al*. [65] reported that significant differences exist between specimens for compressive modulus, mean value is assumed to be reasonable value for the simulation. Properties in Table 4.3 are introduced in the FE model to investigate its

behavior with these skull bone mechanical properties. Boundary and loading conditions remain the same as Figure 4.19.

Following shows the FEA result of the skull model using properties from [65]. The result describes that maximum stress (74MPa) stays below the ultimate strength as well as the principal maximum and minimum strains (9.3E-3 and -10.1E-3 respectively). Thus, topology optimized solutions avoids failure with maximum mastication force.

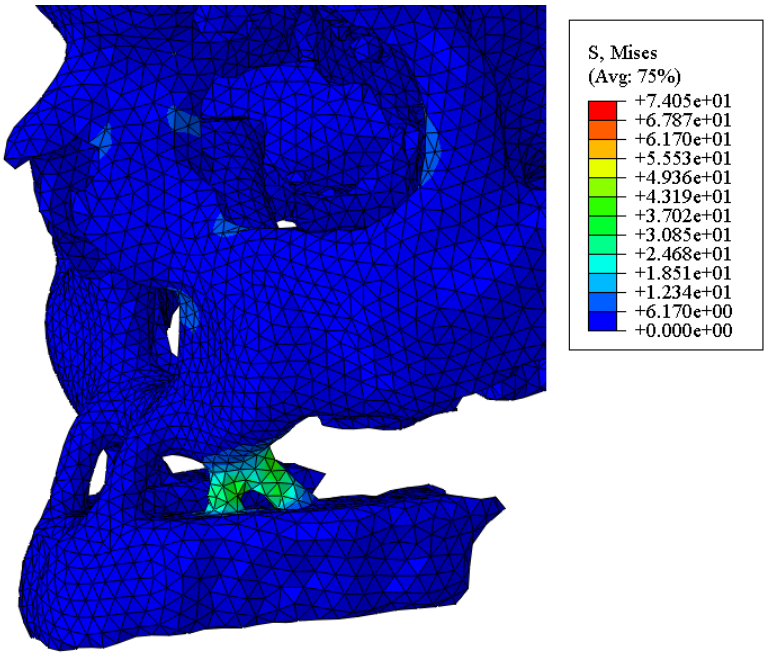

Figure 4.33. Von mises stress of FE model
using isotropic skull bone mechanical property from McElhaney *et al*. [65]

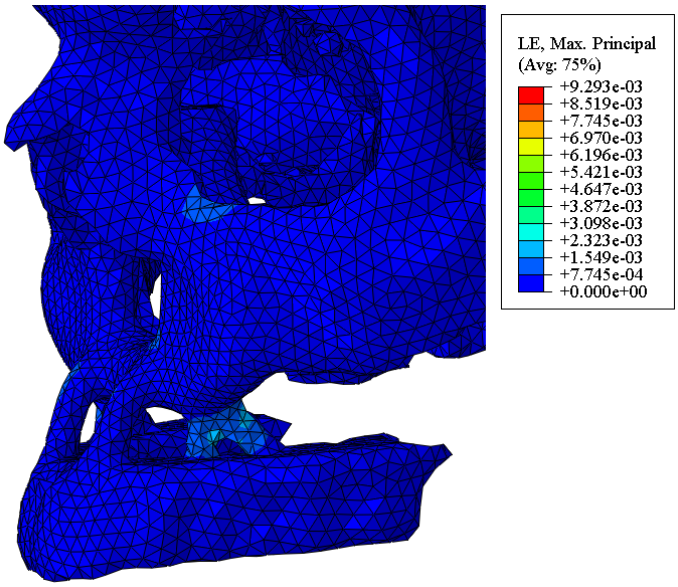

Figure 4.34. Maximum principal strain of FE model using isotropic skull bone mechanical property from McElhaney *et al*. [65]

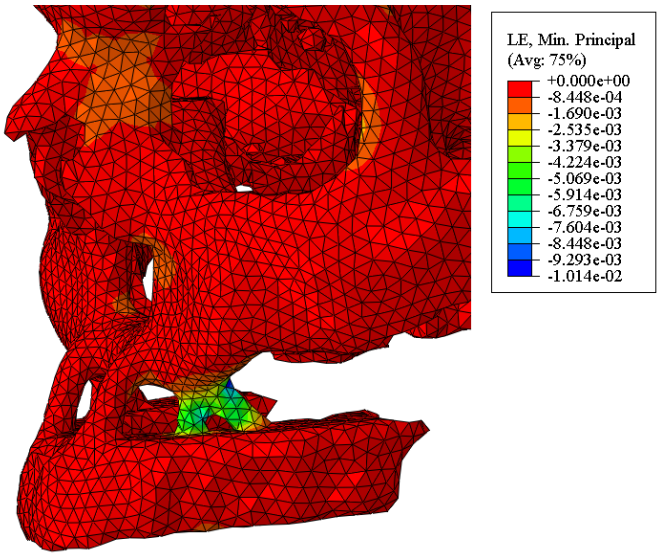

Figure 4.35. Minimum principal strain of FE model using isotropic skull bone mechanical property from McElhaney *et al*. [65]

4.7 Summary

In this chapter, feasibility of one of the topology optimized solutions suggested in Chapter 3 is examined. The skull configuration where bone replacement shapes replaced the region of defect is put into an experiment that simulates human mastication activity with point loads in the molar teeth to explore the mechanical behavior in the most critical region. It is found that load transfer mechanisms are revived as it successfully transfers the load towards the midface. The FEA using material property of ABS plus obtained from experiment (under compression) confirms that the trends follow that of mechanical testing which validates the FEA of skull model. Finally, human skull bone property is used in the FEA whether the topology would survive the maximum mastication force reported i.e. 534N. The result showed that the maximum stress and maximum strains stay below ultimate material properties. Thus, shapes from topology optimization are mechanically feasible solution to replace the region of defect.

Chapter 5 Summary, Conclusion and Future Work

5.1 Summary

This thesis explores the feasibility of topology optimization in craniofacial reconstructive surgery. In chapter 2, the formulations of element based topology optimization are introduced and explained. Multiresolution topology optimization (MTOP) is a new scheme that allows obtaining results with better mesh resolution that is higher than that of the displacement mesh. 2D and 3D numerical examples are presented to show the efficacy of the technique. In chapter 3, this technique is applied to human facial skeleton. A load transfer mechanism (buttress systems) in human facial skeleton is reviewed. Four patient data with defects that destroyed buttress systems are selected. Using multiresolution topology optimization scheme, patient-specific bone replacement shapes are designed. A parametric study of design variables for multiresolution topology optimization is performed. Chapter 4 covers design simulation and experimental validation of bone replacement shapes obtained in Chapter 3. Bone replacement shapes are inserted in the defect region using CAD software. Using 3D printing technology, an implant integrated skull is printed and mechanical testing is performed to see whether it can withstand masticatory force. The behavior of the 3D printing material (ABS plus) is characterized by compressive strength test. Human mastication is simulated in both FEA and mechanical testing. Experimentally obtained material property is used in FEA. The

comparison of results from mechanical testing and FEA of skull model shows that FEA effectively represents the compressive behavior. Also, a load transfer mechanism is observed. When isotropic skull bone mechanical properties from McElhaney *et al*. [65] are implemented in the skull FE model, results indicate that the skull with proposed bone replacement shape withstands maximum human mastication of around 500N.

5.2 Conclusion and Future Work

The present work enabled to derive a conclusion that using topology optimization can be a feasible option to obtain bone replacement shapes for large craniofacial defects. The contributions of this study can be summarized as follows;

- Patient specific bone replacement shapes are generated using topology optimization. Patient specific bone replacement shapes are inserted into the region of defect using Computer Aided Design (CAD) software to simulate surgical insertion.
- One of the skull models is 3D printed via Fused Decomposition Modeling (FDM).
- Material characterization of ABS plus (3D printing material) is performed in compression.
- Finite Element Analysis (FEA) is performed to validate the design to explore mechanical behavior of skull model under masticatory load.
- Fixture is designed to support the skull during testing in CAD and fabricated. Load frame and Digital Image Correlation (DIC) technique is employed.
- Topology optimized solution is confirmed to revive load transfer mechanism in the midface and would withstand maximum mastication force (~500N).

The topology optimization used in this work is designed for minimizing compliance so the algorithm can be applied to many other areas in the skeleton system where bone replacement shapes are required after bone loss. Instead of defects in the midface, it can also be used to handle temporal bone defects after oncologic resection [66] to suggest appropriate replacement shapes. Topology optimization can suggest a structure that would efficiently stiffen the teeth root in the dental fortification process when combined with current restoration techniques.

Multiresolution topology optimization used in this study considers static loads in elastic problem. Dynamic [67] or nonlinear problem [68] should be investigated in the future. Using constitutive modeling for anisotropic material [69] or complex composites [70] may greatly improve the algorithm especially to successfully implement complex nature of bone or to design implants for plastic surgery, e.g. chin augmentation.

In addition, the objective function employed in this study only handles single objective (i.e. minimization of compliance). The objective function can be expanded to cover multiphysics [71-73] or multiscale problems [74, 75] to include various aspects in optimization process. For example, biological and physiological factors can be introduced in the optimization technique for reconstructive surgery if proper material designing scheme is included in the current objective function.

Validation process in present work is limited to elastic deformation of isotropic material. Bone healing, resorption and stress shielding can be taken into consideration. Effect of using non-uniform rational basis spline (NURBS) over polygon mesh used in this study to smoothly represent exact geometry [76] of the object of interest can be also investigated.

Appendix

1. Shape Function Derivatives (B) Matrix

In this section, the derivation of B matrix is presented for a Q4 linear quadrilateral element. Consider Q4 element as follows.

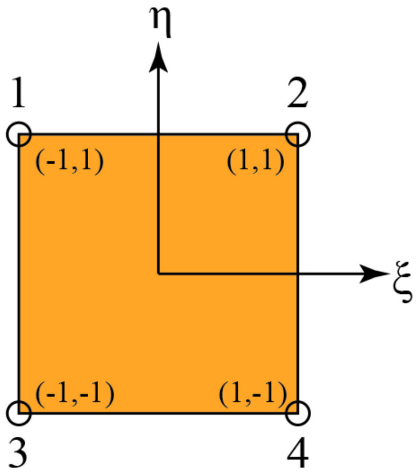

Figure A.1. Standard Q4 element in local coordinate system

Shape functions are the functions which valued 1 at the node and 0 at the others, so following four functions can be established.

$$N_1=\frac{(1-\xi)\cdot(1+\eta)}{4} \qquad N_2=\frac{(1+\xi)\cdot(1-\eta)}{4}$$

$$N_3=\frac{(1+\xi)\cdot(1+\eta)}{4} \qquad N_4=\frac{(1-\xi)\cdot(1-\eta)}{4}$$

These shape functions are used to represent the element displacement in two principal directions.

$$u_{element}=[N][u_{node}]$$

$$u_{element}=\begin{bmatrix}u_x\\u_y\end{bmatrix}=\begin{bmatrix}N_1 & 0 & N_2 & 0 & N_3 & 0 & N_4 & 0\\0 & N_1 & 0 & N_2 & 0 & N_3 & 0 & N_4\end{bmatrix}.\begin{bmatrix}u1_x\\u1_y\\u2_x\\u2_y\\u3_x\\u3_y\\u4_x\\u4_y\end{bmatrix}$$

Element strains can be obtained from derivatives of displacement as follows.

$$[\varepsilon_{element}]=\begin{bmatrix}\varepsilon_x\\\varepsilon_y\\\gamma_{xy}\end{bmatrix}=\begin{bmatrix}\frac{\partial u_x}{\partial x}\\\frac{\partial u_y}{\partial y}\\\frac{\partial u_y}{\partial x}+\frac{\partial u_x}{\partial y}\end{bmatrix}=[\nabla N][u_{node}]=\begin{bmatrix}\frac{\partial}{\partial x} & 0\\0 & \frac{\partial}{\partial y}\\\frac{\partial}{\partial y} & \frac{\partial}{\partial x}\end{bmatrix}[N][u_{node}]$$

$$[\varepsilon_{element}]=\begin{bmatrix}\frac{\partial N_1}{\partial x} & 0 & \frac{\partial N_2}{\partial x} & 0 & \frac{\partial N_3}{\partial x} & 0 & \frac{\partial N_4}{\partial x} & 0\\0 & \frac{\partial N_1}{\partial y} & 0 & \frac{\partial N_2}{\partial y} & 0 & \frac{\partial N_3}{\partial y} & 0 & \frac{\partial N_4}{\partial y}\\\frac{\partial N_1}{\partial y} & \frac{\partial N_1}{\partial x} & \frac{\partial N_2}{\partial y} & \frac{\partial N_2}{\partial x} & \frac{\partial N_3}{\partial y} & \frac{\partial N_3}{\partial x} & \frac{\partial N_4}{\partial y} & \frac{\partial N_4}{\partial x}\end{bmatrix}.\begin{bmatrix}u1_x\\u1_y\\u2_x\\u2_y\\u3_x\\u3_y\\u4_x\\u4_y\end{bmatrix}$$

$$[\nabla N] = \begin{bmatrix} \frac{\partial N_1}{\partial x} & 0 & \frac{\partial N_2}{\partial x} & 0 & \frac{\partial N_3}{\partial x} & 0 & \frac{\partial N_4}{\partial x} & 0 \\ 0 & \frac{\partial N_1}{\partial y} & 0 & \frac{\partial N_2}{\partial y} & 0 & \frac{\partial N_3}{\partial y} & 0 & \frac{\partial N_4}{\partial y} \\ \frac{\partial N_1}{\partial y} & \frac{\partial N_1}{\partial x} & \frac{\partial N_2}{\partial y} & \frac{\partial N_2}{\partial x} & \frac{\partial N_3}{\partial y} & \frac{\partial N_3}{\partial x} & \frac{\partial N_4}{\partial y} & \frac{\partial N_4}{\partial x} \end{bmatrix}$$

Taking coordinate transformation into account, chain rule is applied to obtain $\frac{\partial N_1}{\partial x}$.

$$\frac{\partial N_1}{\partial x} = \frac{\partial N_1}{\partial \xi} \cdot \frac{\partial \xi}{\partial x} = \frac{\partial N_1}{\partial \xi} \cdot \left(\frac{\partial x}{\partial \xi}\right)^{-1}$$

$$[B] = \begin{bmatrix} \frac{\partial N_1}{\partial \xi} & 0 & \frac{\partial N_2}{\partial \xi} & 0 & \frac{\partial N_3}{\partial \xi} & 0 & \frac{\partial N_4}{\partial \xi} & 0 \\ 0 & \frac{\partial N_1}{\partial \eta} & 0 & \frac{\partial N_2}{\partial \eta} & 0 & \frac{\partial N_3}{\partial \eta} & 0 & \frac{\partial N_4}{\partial \eta} \\ \frac{\partial N_1}{\partial \eta} & \frac{\partial N_1}{\partial \xi} & \frac{\partial N_2}{\partial \eta} & \frac{\partial N_2}{\partial \xi} & \frac{\partial N_3}{\partial \eta} & \frac{\partial N_3}{\partial \xi} & \frac{\partial N_4}{\partial \eta} & \frac{\partial N_4}{\partial \xi} \end{bmatrix} \cdot \frac{1}{J}$$

$$[B] = \begin{bmatrix} -(1+\eta) & 0 & 1+\eta & 0 & 1-\eta & 0 & -(1-\eta) & 0 \\ 0 & 1-\xi & 0 & 1+\xi & 0 & -(1+\xi) & 0 & -(1-\xi) \\ 1-\xi & -(1+\eta) & 1+\xi & 1+\eta & -(1+\xi) & 1-\eta & -(1-\xi) & -(1-\eta) \end{bmatrix} \cdot \frac{1}{J}$$

For non-dimensional problems, J=1.

2. Material Property (D) Matrix

In this section, the derivation of D matrix is presented for plane stress. Consider a plane stress as follows.

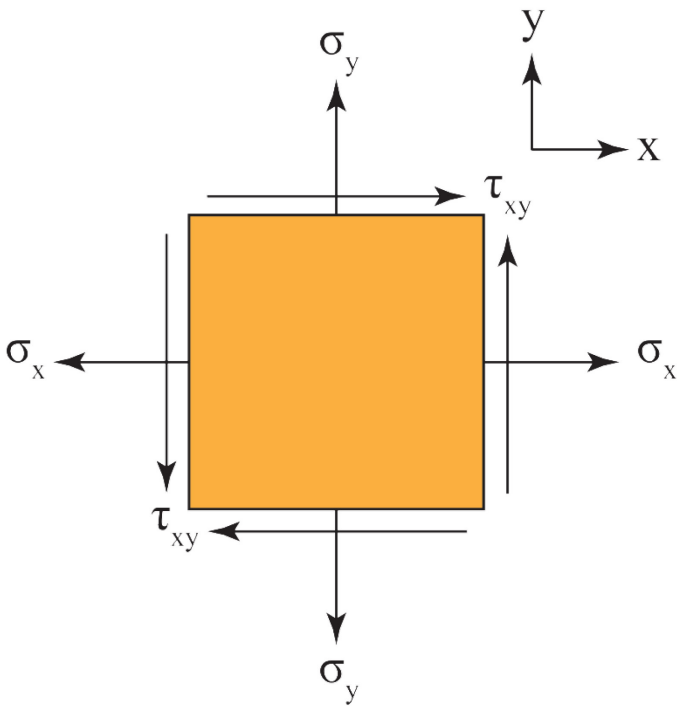

Figure A.2. Plane stress example

Strains are calculated based on stress and material properties.

$$\varepsilon_x = \frac{\sigma_x}{E} - \nu\frac{\sigma_y}{E} \qquad \varepsilon_y = \frac{\sigma_y}{E} - \nu\frac{\sigma_x}{E} \qquad \gamma_{xy} = \frac{\tau_{xy}}{G}$$

where ν is the Poisson's ratio, E, and G are the Young's and Shear modulus respectively. Matrix representation of three equations above is presented as follows.

$$\begin{bmatrix} \varepsilon_x \\ \varepsilon_y \\ \gamma_{xy} \end{bmatrix} = \frac{1}{E} \cdot \begin{bmatrix} 1 & -\nu & 0 \\ -\nu & 1 & 0 \\ 0 & 0 & E/G \end{bmatrix} \begin{bmatrix} \sigma_x \\ \sigma_y \\ \tau_{xy} \end{bmatrix}$$

Now, relocating stress and strain allows getting material property matrix for stiffness K.

$$\begin{bmatrix} \sigma_x \\ \sigma_y \\ \tau_{xy} \end{bmatrix} = \frac{E}{1-\nu^2} \cdot \begin{bmatrix} 1 & \nu & 0 \\ \nu & 1 & 0 \\ 0 & 0 & (1-\nu)/2 \end{bmatrix} \begin{bmatrix} \varepsilon_x \\ \varepsilon_y \\ \gamma_{xy} \end{bmatrix}$$

$$\mathbf{D} = \frac{E}{1-\nu^2} \begin{bmatrix} 1 & \nu & 0 \\ \nu & 1 & 0 \\ 0 & 0 & (1-\nu)/2 \end{bmatrix}$$

References

[1] O. Sigmund, "Topology optimization: a tool for the tailoring of structures and materials," *Philosophical Transactions of the Royal Society of London Series a-Mathematical Physical and Engineering Sciences,* vol. 358, Jan 15 2000.

[2] L. Krog, A. Tucker, M. Kemp, and R. Boyd, "Topology optimization of aircraft wing box ribs," presented at the The Altair Technology Conference 2004, Troy, Michigan, 2004.

[3] M. P. Bendsoe and N. Kikuchi, "Generating optimal topologies in structural design using a homogenization method," *Computer Methods in Applied Mechanics and Engineering,* vol. 71, Nov 1988.

[4] M. P. Bendsoe and O. Sigmund, *Topology Optimization Theory, Methods and Applications*. Berlin: Springer, 2003.

[5] K. Suzuki and N. Kikuchi, "A homogenization method for shape and topology optimization," *Computer Methods in Applied Mechanics and Engineering,* vol. 93, pp. 291-318, Dec 1991.

[6] M. Zhou and G. I. N. Rozvany, "The COC algorithm .2. Topological, geometrical and generalized shape optimization," *Computer Methods in Applied Mechanics and Engineering,* vol. 89, pp. 309-336, Aug 1991.

[7] M. P. Bendsoe and O. Sigmund, "Material interpolation schemes in topology optimization," *Archive of Applied Mechanics,* vol. 69, Nov 1999.

[8] O. Sigmund and J. Petersson, "Numerical instabilities in topology optimization: A survey on procedures dealing with checkerboards, mesh-dependencies and local minima," *Structural Optimization,* vol. 16, pp. 68-75, Aug 1998.

[9] T. Borrvall and J. Petersson, "Large-scale topology optimization in 3D using parallel computing," *Computer Methods in Applied Mechanics and Engineering,* vol. 190, pp. 6201-6229, 2001.

[10] A. Mahdavi, R. Balaji, M. Frecker, and E. M. Mockensturm, "Topology optimization of 2D continua for minimum compliance using parallel computing," *Structural and Multidisciplinary Optimization,* vol. 32, pp. 121-132, Aug 2006.

[11] O. Amir, M. P. Bendsoe, and O. Sigmund, "Approximate reanalysis in topology optimization," *International Journal for Numerical Methods in Engineering,* vol. 78, pp. 1474-1491, Jun 18 2009.

[12] O. Amir and O. Sigmund, "On reducing computational effort in topology optimization: how far can we go?," *Structural and Multidisciplinary Optimization,* vol. 44, pp. 25-29, Jul 2011.

[13] O. Amir, M. Stolpe, and O. Sigmund, "Efficient use of iterative solvers in nested topology optimization," *Structural and Multidisciplinary Optimization,* vol. 42, pp. 55-72, Jul 2010.

[14] J. K. Guest, J. H. Prevost, and T. Belytschko, "Achieving minimum length scale in topology optimization using nodal design variables and projection functions," *International Journal for Numerical Methods in Engineering,* vol. 61, pp. 238-254, Sep 2004.

[15] K. Matsui and K. Terada, "Continuous approximation of material distribution for topology optimization," *International Journal for Numerical Methods in Engineering,* vol. 59, pp. 1925-1944, Apr 2004.

[16] G. H. Paulino and C. H. Le, "A modified Q4/Q4 element for topology optimization," *Structural and Multidisciplinary Optimization,* vol. 37, pp. 255-264, Jan 2009.

[17] S. J. Hollister, "Scaffold design and manufacturing: From concept to clinic," *Advanced Materials,* vol. 21, Sep 4 2009.

[18] S. J. Hollister, R. D. Maddox, and J. M. Taboas, "Optimal design and fabrication of scaffolds to mimic tissue properties and satisfy biological constraints," *Biomaterials,* vol. 23, pp. 4095-4103, Oct 2002.

[19] T. Adachi, Y. Osako, M. Tanaka, M. Hojo, and S. J. Hollister, "Framework for optimal design of porous scaffold microstructure by computational simulation of bone regeneration," *Biomaterials,* vol. 27, pp. 3964-3972, Jul 2006.

[20] V. J. Challis, A. P. Roberts, J. F. Grotowski, L.-C. Zhang, and T. B. Sercombe, "Prototypes for bone implant scaffolds designed via topology optimization and manufactured by solid freeform fabrication," *Advanced Engineering Materials,* vol. 12, pp. 1106-1110, Nov 2010.

[21] S. J. Hollister, C. Y. Lin, E. Saito, R. D. Schek, J. M. Taboas, J. M. Williams*, et al.*, "Engineering craniofacial scaffolds," *Orthodontics & craniofacial research,* vol. 8, Aug 2005.

[22] S. J. Hollister and C. Y. Lin, "Computational design of tissue engineering scaffolds," *Computer Methods in Applied Mechanics and Engineering,* vol. 196, 2007.

[23] H. Kang, C.-Y. Lin, and S. J. Hollister, "Topology optimization of three dimensional tissue engineering scaffold architectures for prescribed bulk modulus and diffusivity," *Structural and Multidisciplinary Optimization,* vol. 42, pp. 633-644, Oct 2010.

[24] C. Y. Lin, N. Kikuchi, and S. J. Hollister, "A novel method for biomaterial scaffold internal architecture design to match bone elastic properties with desired porosity," *Journal of Biomechanics,* vol. 37, pp. 623-636, May 2004.

[25] Y. Chen, S. Zhou, and Q. Li, "Microstructure design of biodegradable scaffold and its effect on tissue regeneration," *Biomaterials,* vol. 32, pp. 5003-5014, Aug 2011.

[26] R. C. Schultz, *Facial Injuries*. Chicago, IL USA: Year Book Medical Publisher, Inc, 1970.

[27] A. Sutradhar, G. H. Paulino, M. J. Miller, and T. H. Nguyen, "Topological optimization for designing patient-specific large craniofacial segmental bone replacements," *Proceedings of the National Academy of Sciences of the United States of America,* vol. 107, Jul 27 2010.

[28] B. Bourdin, "Filters in topology optimization," *International Journal for Numerical Methods in Engineering,* vol. 50, pp. 2143-2158, Mar 2001.

[29] T. H. Nguyen, G. H. Paulino, J. Song, and C. H. Le, "A computational paradigm for multiresolution topology optimization (MTOP)," *Structural and Multidisciplinary Optimization,* vol. 41, Apr 2010.

[30] G. I. N. Rozvany, "A critical review of established methods of structural topology optimization," *Structural and Multidisciplinary Optimization,* vol. 37, Jan 2009.

[31] K. Svanberg, "The method of moving asymtotes - A new method for structural optimization," *International Journal for Numerical Methods in Engineering,* vol. 24, pp. 359-373, Feb 1987.

[32] M. P. Bendsoe, *Optimization of Structural Topology, Shape, and Material*. Berlin: Springer, 1995.

[33] S. Wang, E. de Sturler, and G. H. Paulino, "Large-scale topology optimization using preconditioned Krylov subspace methods with recycling," *International*

Journal for Numerical Methods in Engineering, vol. 69, pp. 2441-2468, Mar 19 2007.

[34] S. F. Rahmatalla and C. C. Swan, "A Q4/Q4 continuum structural topology optimization implementation," *Structural and Multidisciplinary Optimization,* vol. 27, pp. 130-135, May 2004.

[35] E. M. Genden, "Reconstruction of the mandible and the maxilla. The evolution of surgical technique," *Archives of Facial Plastic Surgery,* vol. 12, pp. 87-90, Mar-Apr 2010.

[36] N. D. Futran and E. Mendez, "Developments in reconstruction of midface and maxilla," *Lancet Oncology,* vol. 7, pp. 249-258, Mar 2006.

[37] P. Andrades, O. Militsakh, M. M. Hanasono, J. Rieger, and E. L. Rosenthal, "Current strategies in reconstruction of maxillectomy defects," *Archives of Otolaryngology-Head & Neck Surgery,* vol. 137, pp. 806-812, Aug 2011.

[38] Y. Shen, J. Sun, J. Li, M.-m. Li, W. Huang, and A. Ow, "Special considerations in virtual surgical planning for secondary accurate maxillary reconstruction with vascularised fibula osteomyocutaneous flap," *Journal of Plastic Reconstructive and Aesthetic Surgery,* vol. 65, pp. 893-902, Jul 2012.

[39] A. K. Antony, W. F. Chen, A. Kolokythas, K. A. Weimer, and M. N. Cohen, "Use of virtual surgery and stereolithography-guided osteotomy for mandibular reconstruction with the free fibula," *Plastic and Reconstructive Surgery,* vol. 128, pp. 1080-1084, Nov 2011.

[40] Y. He, H. G. Zhu, Z. Y. Zhang, J. He, and R. Sader, "Three-dimensional model simulation and reconstruction of composite total maxillectomy defects with fibula osteomyocutaneous flap flow-through from radial forearm flap," *Oral Surgery Oral Medicine Oral Pathology Oral Radiology and Endodontology,* vol. 108, pp. E6-E12, Dec 2009.

[41] C. M. McCarthy and P. G. Cordeiro, "Microvascular reconstruction of oncologic defects of the midface," *Plastic and Reconstructive Surgery,* vol. 126, pp. 1947-1959, Dec 2010.

[42] R. Bluebond-Langner and E. D. Rodriguez, "Application of skeletal buttress analogy in composite facial reconstruction," *Craniomaxillofacial trauma & reconstruction,* vol. 2, pp. 19-25, Mar 2009.

[43] P. G. Cordeiro and C. M. Chen, "A 15-year review of midface reconstruction after total and subtotal maxillectomy: Part II. Technical modifications to maximize aesthetic and functional outcomes," *Plastic and Reconstructive Surgery,* vol. 129, pp. 139-147, Jan 2012.

[44] E. L. DuBrul, *Sicher and DuBrul's Oral anatomy*, 8th Edition ed.: Ishiyaku EuroAmerica, 1988.

[45] R. H. Rudderman and R. L. Mullen, "Biomechanics of the facial skeleton," *Clinics in Plastic Surgery,* vol. 19, pp. 11-29, Jan 1992.

[46] P. N. Manson, J. E. Hoopes, and C. T. Su, "Structural pillars of the facial skeleton - An approach to the management of Le Fort fractures," *Plastic and Reconstructive Surgery,* vol. 66, pp. 54-61, 1980.

[47] Y. Yamamoto, K. Kawashima, T. Sugihara, K. Nohira, Y. Furuta, and S. Fukuda, "Surgical management of maxillectomy defects based on the concept of buttress reconstruction," *Head and Neck-Journal for the Sciences and Specialties of the Head and Neck,* vol. 26, pp. 247-256, Mar 2004.

[48] R. Hilloowala and H. Kanth, "The transmission of masticatory forces and nasal septum: Structural comparison of the human skull and gothic cathedral," *Cranio-the Journal of Craniomandibular Practice,* vol. 25, pp. 166-171, Jul 2007.

[49] P. W. Flint, B. H. Haughey, V. J. Lund, J. K. Niparko, M. A. Richardson, K. T. Robbins*, et al.*, *Cummings Otolaryngology - Head and Neck Surgery*, 5th edition ed.: Elsevier Health Sciences, 2010.

[50] J. S. Gruss and S. E. Mackinnon, "Complex maxillary fractures - Role of buttress reconstruction and immediate bone-grafts," *Plastic and Reconstructive Surgery,* vol. 78, pp. 9-22, Jul 1986.

[51] T. Nagasao, T. Nakajima, A. Kimura, T. Kaneko, H. M. Jin, and T. Tamaki, "The dynamic role of buttress reconstruction after maxillectomy," *Plastic and Reconstructive Surgery,* vol. 115, pp. 1328-1340, Apr 15 2005.

[52] Z. I. Berlin and V. S. Group, "Amira," 5.4.3 ed. Burlington, Massachusetts: VSG, an FEI Company, 2012.

[53] I. Tecplot, "Tecplot 360," 2009 ed. Bellevue, Washington: Tecplot, Inc., 2009.

[54] M. Wehmoller, S. Weihe, C. Rasche, P. Scherer, and H. Eufinger, "CAD/CAM-prefabricated titanium implants for large skull defects - clinical experience with 166 patients from 1994 to 2000," *Cars 2004: Computer Assisted Radiology and Surgery, Proceedings,* vol. 1268, pp. 667-672, 2004.

[55] A. J. Gil, R. V. Curtis, J. Bonet, and T. Coward, "Finite element superplastic forming (FE-SPF) of patient-specific maxillofacial prostheses," *International Journal for Numerical Methods in Biomedical Engineering,* vol. 26, pp. 139-155, Jan 2010.

[56] E. P. Kavanagh, C. Frawley, G. Kearns, F. Wallis, T. McGloughlin, and J. Jarvis, "Use of finite element analysis in presurgical planning: treatment of mandibular fractures," *Irish Journal of Medical Science,* vol. 177, pp. 325-331, Dec 2008.

[57] N. L. Clelland, J. D. Seidt, L. G. Dias Daroz, and E. A. McGlumphy, "Comparison of strains for splinted and nonsplinted implant prostheses using

three-dimensional image correlation," *International Journal of Oral & Maxillofacial Implants,* vol. 25, pp. 953-959, Sep-Oct 2010.

[58] R. Zdero and H. Bougherara, *Orthopaedic Biomechanics: A Practical Approach to Combining Mechanical Testing and Finite Element Analysis*. Rijeka, Croatia: Sciyo, 2010.

[59] R. Petzold, H. F. Zeilhofer, and W. A. Kalender, "Rapid prototyping technology in medicine - basics and applications," *Computerized Medical Imaging and Graphics,* vol. 23, pp. 277-284, Sep-Oct 1999.

[60] M. Robiony, I. Salvo, F. Costa, N. Zerman, M. Bazzocchi, F. Toso*, et al.*, "Virtual reality surgical planning for maxillofacial distraction osteogenesis: The role of reverse engineering rapid prototyping and cooperative work," *Journal of Oral and Maxillofacial Surgery,* vol. 65, pp. 1198-1208, Jun 2007.

[61] Zureks. (2008, Dec 21). *Fused Decomposition Modelling*. Available: http://en.wikipedia.org/wiki/Fused_deposition_modeling

[62] G. E. Carlsson, "Bite force and chewing efficiency," *Frontiers of oral physiology,* vol. 1, pp. 265-92, 1974.

[63] J. J. Thomason, A. P. Russell, and M. Morgeli, "Forces of biting, body size, and masticatory muscle tension in the opossum didelphis-Virginiana," *Canadian Journal of Zoology-Revue Canadienne De Zoologie,* vol. 68, pp. 318-324, Feb 1990.

[64] D. Systèmes, "ABAQUS," 6.10-1 ed. Province, Rhode Island, USA: Simuilia, 2010.

[65] McElhaney.Jh, J. L. Fogle, J. W. Melvin, R. R. Haynes, V. L. Roberts, and N. M. Alem, "Mechanical properties of cranial bone," *Journal of Biomechanics,* vol. 3, pp. 495, 1970.

[66] M. M. Hanasono, A. K. Silva, P. Yu, R. J. Skoracki, E. M. Sturgis, and P. W. Gidley, "Comprehensive management of temporal bone defects after oncologic resection," *Laryngoscope,* vol. 122, pp. 2663-2669, Dec 2012.

[67] W. M. Rubio, E. C. N. Silva, and G. H. Paulino, "Toward Optimal Design of Piezoelectric transducers based on multifunctional and smoothly graded hybrid material systems," *Journal of Intelligent Material Systems and Structures,* vol. 20, pp. 1725-1746, Sep 2009.

[68] H. S. Jung and S. Cho, "Reliability-based topology optimization of geometrically nonlinear structures with loading and material uncertainties," *Finite Elements in Analysis and Design,* vol. 41, pp. 311-331, Dec 2004.

[69] S. Li and S. N. Atluri, "The MLPG mixed collocation method for material orientation and topology optimization of anisotropic solids and structures," *Cmes-Computer Modeling in Engineering & Sciences,* vol. 30, pp. 37-56, Jun 2008.

[70] N. de Kruijf, S. Zhou, Q. Li, and Y.-W. Mai, "Topological design of structures and composite materials with multiobjectives," *International Journal of Solids and Structures,* vol. 44, pp. 7092-7109, Nov 2007.

[71] O. Sigmund, "Design of multiphysics actuators using topology optimization - Part II: Two-material structures," *Computer Methods in Applied Mechanics and Engineering,* vol. 190, 2001 2001.

[72] J. A. Madeira, H. C. Rodrigues, and H. Pina, "Multiobjective topology optimization of structures using genetic algorithms with chromosome repairing," *Structural and Multidisciplinary Optimization,* vol. 32, pp. 31-39, Jul 2006.

[73] J. Lin, Z. Luo, and L. Tong, "A new multi-objective programming scheme for topology optimization of compliant mechanisms," *Structural and Multidisciplinary Optimization,* vol. 40, Jan 2010.

[74] C. S. Andreasen and O. Sigmund, "Multiscale modeling and topology optimization of poroelastic actuators," *Smart Materials and Structures,* vol. 21, Jun 2012.

[75] R. C. Carbonari, E. C. N. Silva, and G. H. Paulino, "Multi-actuated functionally graded piezoelectric micro-tools design: A multiphysics topology optimization approach," *International Journal for Numerical Methods in Engineering,* vol. 77, pp. 301-336, Jan 15 2009.

[76] T. J. R. Hughes, J. A. Cottrell, and Y. Bazilevs, "Isogeometric analysis: CAD, finite elements, NURBS, exact geometry and mesh refinement," *Computer Methods in Applied Mechanics and Engineering,* vol. 194, pp. 4135-4195, 2005.